Theses and Dissertations--Mechanical Engineering

Mechanical Engineering

2015

Modeling of spallation phenomenon in an arc-jet environment

Raghava Sai Chaitanya Davuluri

University of Kentucky, raghava.sai.chaitanya@gmail.com

STUDENT AGREEMENT:

I represent that my thesis or dissertation and abstract are my original work. Proper attribution has been given to all outside sources. I understand that I am solely responsible for obtaining any needed copyright permissions. I have obtained needed written permission statement(s) from the owner(s) of each third-party copyrighted matter to be included in my work, allowing electronic distribution (if such use is not permitted by the fair use doctrine) which will be submitted to UKnowledge as Additional File.

I hereby grant to The University of Kentucky and its agents the irrevocable, non-exclusive, and royalty-free license to archive and make accessible my work in whole or in part in all forms of media, now or hereafter known. I agree that the document mentioned above may be made available immediately for worldwide access unless an embargo applies.

I retain all other ownership rights to the copyright of my work. I also retain the right to use in future works (such as articles or books) all or part of my work. I understand that I am free to register the copyright to my work.

REVIEW, APPROVAL AND ACCEPTANCE

The document mentioned above has been reviewed and accepted by the student's advisor, on behalf of the advisory committee, and by the Director of Graduate Studies (DGS), on behalf of the program; we verify that this is the final, approved version of the student's thesis including all changes required by the advisory committee. The undersigned agree to abide by the statements above.

Raghava Sai Chaitanya Davuluri, Student

Dr. Alexandre Martin, Major Professor

Dr. Haluk E. Karaca, Director of Graduate Studies

Modeling of spallation phenomenon in an arc-jet environment

THESIS

A thesis submitted in partial

fulfillment of the requirements for

the degree of Master of Science in

Mechanical Engineering in the

College of Engineering at the

University of Kentucky

By

Raghava Sai Chaitanya Davuluri

Lexington, Kentucky

Director: Dr. Alexandre Martin, Assistant Professor of Mechanical Engineering

Lexington, Kentucky 2015

ABSTRACT OF THESIS

Modeling of spallation phenomenon in an arc-jet environment

Space vehicles, while entering the planetary atmosphere, experience high loads of heat. Ablative materials are commonly used for a thermal protection system, which undergo mass removal mechanisms to counter the heat rates. Spallation is one of the ablative processes, which is characterized by the ejection of solid particles from the material into the flow. Numerical codes that are used in designing the heat shields ignore this phenomenon. Hence, to evaluate the effectiveness of spallation phenomenon, a numerical model is developed to compute the dynamics and chemistry of the particles. The code is one-way coupled to a CFD code that models high enthalpy flow field around a lightweight ablative material. A parametric study is carried out to examine the variations in trajectories with respect to ejection parameters. Numerical results are presented for argon and air flow fields, and their effect on the particle behavior is studied. The spallation code is loosely coupled with the CFD code to evaluate the impact of a particle on the flow field, and a numerical study is conducted.

KEYWORDS: atmospheric entry, thermal protection system, ablation, spallation

Author's signature: <u>Raghava Sai Chaitanya Davuluri</u>

Date: <u>August 6, 2015</u>

Modeling of spallation phenomenon in an arc-jet environment

By

Raghava Sai Chaitanya Davuluri

Director of Thesis:____Dr. Alexandre Martin___

Director of Graduate Studies:____Dr. Haluk E. Karaca___

Date:_____August 6, 2015___

Dedicated to Amma and Nānna

ACKNOWLEDGMENTS

CONTENTS

LIST OF FIGURES

Chapter 1 Introduction

1.1   Background

Mankind has always been interested in unveiling the mysteries of the universe, and space exploration is a recent example of this interest. These missions range from exploring celestial bodies, to performing micro-gravity experiments in the International Space Station (ISS). Vehicles required for the planetary missions are prepared based on the set of requirements needed to fulfill the specific goals. The entry phase stands as one of the most critical requirements, in bringing the vehicle into the planetary atmosphere. In order to successfully enter the atmosphere, the vehicle needs to balance three requisites: deceleration, heating, and accuracy of landing [1]. The vehicle enters at hypersonic speeds and is maneuvered in a trajectory to land at designated area. At the same time, it decelerates to ensure the safety of the payload. The kinetic energy of the vehicle entering the planetary atmosphere is dissipated mainly in the form of heat. Though most of the heat is rejected to the atmosphere, a fraction of this energy reaches the surface of the vehicle, based on its aerodynamic shape, through convection and radiation. The vehicle is equipped with a Thermal Protection System (TPS) which counters the high heat rates by blocking, absorbing, or radiating it and thereby providing safety to the payload. Figure 1.1 depicts the artistic interpretation of SpaceX Dragon capsule's re-entry into the earth's atmosphere.

The high heat rates during the re-entry cause extreme temperatures in the shock layer which lead to the dissociation of atmospheric gas molecules. Based on the catalytic nature of TPS, the dissociated atoms encourage the recombination of boundary layer species thereby, releasing the heat of dissociation and enhancing heating at the surface. Also, the boundary layer gases react chemically with the surface leading to its recession. Hence, the TPS should

Figure 1.1: SpaceX Dragon Capsule Re-entry

(Courtesy of SpaceX [2])

have a low tendency to catalyze the chemical reactions and protect the vehicle during catalytic heating [3]. There are various types of Thermal Protection Systems: the Radiative System, Heat-Sink System, Transpiration and Film Cooling System, Ablative System, and Convective Cooling System. For planetary exploration, ablative TPS are most widely used, because of its satisfactory performance, light weight, relative simplicity and reliability.

Ablative TPS materials protect the vehicle from high heat rates by undergoing following chemical and physical processes: subliming, oxidizing, melting-vaporizing, and charring [4]. These materials are used on space vehicles, ballistic-missile entry vehicles, and various research vehicles. The choice of material depends on surface heat-rates, surface shear, and pressure gradients. Charring ablators being light weight materials are used in a wide range of entry conditions. These ablators are made up of thermosetting resin such as phenolics, epoxies, or silicones. They may also be reinforced with materials like nylon, or refractories like glass, asbestos, or graphite [5]. The silicone charring ablators are used for low heat

fluxes (surface temperatures less than 1950 K) whereas carbonaceous charring ablators are used for high heat fluxes. These charring ablators are important for research and development as they are used at the locations where the vehicle experiences high surface heating. For example, the charring ablators cover the nose-cone region in ballistic missiles, and the forebody region of the space capsule and probes.

The ablative effectiveness is directly proportional to the density of the material, in contrast to the insulation that is inversely proportional. Hence, with the increase in either heat fluxes, stagnation pressure, or both encountered by the vehicle during re-entry, the selection of materials changes from low to high density [6, 7]. Some of the charring ablator materials used for various space missions are Carbon Phenolic, Phenolic Impregnated Carbon Ablator (PICA), Avcoat, Advanced Carbon-Carbon (ACC), Super Lightweight Ablator (SLA), Norcoat Liège, Asterm, Monolithic Ablator (MonA) and Silicone Impregnated Reusable Ceramic Ablator (SIRCA). Various versions of carbon phenolics were developed to be used in space missions. The *heritage* carbon phenolic was used as TPS for the Pioneer-Venus and Galileo Probes. Also, carbon phenolic was used as a forebody TPS for Hayabusa (MUSES-C) [8, 9], an asteroid explorer by JAXA[1], as well as for the Crew module Atmospheric Re-entry Experiment (CARE), a sub-orbital re-entry mission by ISRO[2]. In the mid 90's, NASA[3] developed PICA and SIRCA. PICA was used as forebody TPS for Mars Science Laboratory (MSL) aeroshell and the Stardust Return Capsule [10, 11, 12]. Similarly, SIRCA was used as a backshell TPS for the Mars Pathfinder [13, 14] and Mars rover missions. Avcoat, a mid-density material, was developed by Textron and employed as a heatshield on the Apollo Command Module and the Orion Crew Exploration Vehicle. ACC along with carbon fibrous insulation, developed by Lockheed-Martin, was used as a forebody TPS on the Genesis capsule. SLA developed by NASA was used as a heat shield in the Viking mission. Also, JAXA is developing SLA [15, 16] to be used for re-entry missions. Similarly, Norcoat Liège devel-

---

[1]Japan Aerospace Exploration Agency
[2]Indian Space Research Organisation
[3]National Aeronautics and Space Administration

3

oped by Astrium-ST was used as a forebody TPS for Atmospheric Re-entry Demonstrator (ARD) [17], as well as the Beagle 2 probe [18] and will be used for the future ExoMars Mission [19]. Other low-density ablators include Asterm (developed by Airbus Defense and Space), and MonA (developed by Lockheed-Martin UK Ampthill) [20, 21, 22, 23], both of which are used for re-entry missions by ESA[4]. Figure 1.2 illustrates different space capsules used for sample re-entry missions.

The ablative TPS counters high heat rates during the atmospheric entry by undergoing several mass-removal mechanisms, collectively called ablation. The ablation phenomenon can be broadly classified into pyrolysis, thermo-chemical ablation, and thermo-mechanical ablation. Figure 1.3 shows different mechanisms taking place in non-ablative and ablative TPS material when subjected to high loads of heat. Pyrolysis is defined as a phenomenon in which the material is heated until it reaches a certain temperature (known as pyrolysis temperature) where it decomposes (pyrolyzes) to carbonaceous residue and releases gas. The pyrolysis zone expands into the material as it gets more heated, and decomposition takes place below the surface. Here, the pyrolysis temperature is a function of local pressure and chemical composition near the surface. The released gas diffuses through the porous char towards the surface and chemically reacts with the near-surface gas.

Due to high temperatures, entry flows are in a weakly ionized thermo-chemical non-equilibrium state. Thermo-chemical ablation is a mechanism in which material reacts with chemical species in the flow (e.g. oxidation, nitridation) or undergoes sublimation forming chemical products, thus triggering material-recession. The nature of the chemical reactions depends on the surface temperatures. At temperatures below 1100 K, the chemical reactions follow reaction-rate kinetics. As the temperatures increase, the chemical reaction rates increase exponentially until the chemical species totally depletes. At even higher temperatures, the chemical reactions are dependent on the diffusion rates of chemical species through the boundary layer. Finally, the sublimation of char occurs at temperatures above 3600 K [4].

---

[4]European Space Agency

(a) Stardust Capsule After Re-entry
(Courtesy of NASA [24])

(b) Hayabusa Capsule After Re-entry
(Courtesy of JAXA [25])
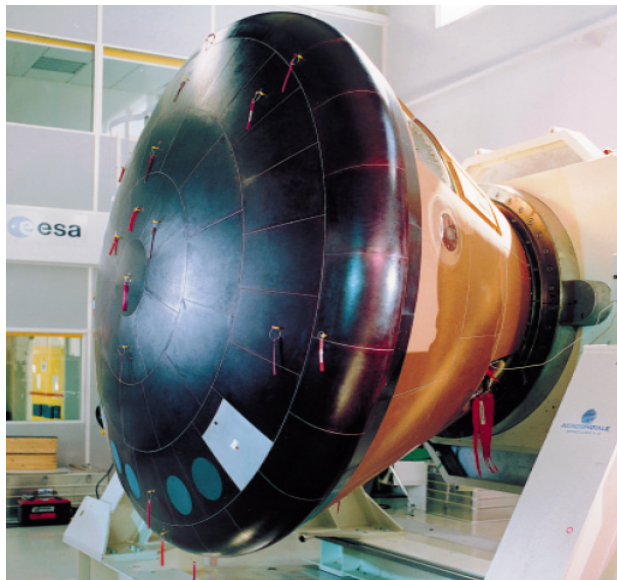
(c) ARD Heat shield
(Copyright © ESA/AEROSPATIALE [17])

(d) CARE Capsule After Re-entry
(Courtesy of ISRO [26])

Figure 1.2: Various Re-entry probes for their respective missions

The char formed is usually weak and brittle, and is subjected to mechanical shear, as well as thermal and internal pressure stresses, which result in the material recession. Mass removal due to spallation is part of thermo-mechanical ablation.

The heating environment and ablation behavior of heat shields have been extensively studied, both theoretically and experimentally. Various computer codes have been developed to numerically simulate the ablation mechanisms [28]. These codes are used to predict the thickness of the heat shield required to accommodate the entry heat rates [29]. However, spallation is disregarded and included in the form of safety margin in these codes. Material Response codes, like the ones used by NASA to design TPS, account for mass removal due to spallation by introducing an empirically determined parameter [30]. There is a need to evaluate the spallation phenomenon for its role in ablation to ensure the design of an efficient light-weight TPS.

1.2 Spallation

Spallation is a form of thermo-mechanical ablation. It is a phenomenon by which the ablative material loses mass in the form of particle ejections. The exact phenomena responsible for the production of spalled particles are not well understood, or even identified. Most likely, these particles are produced by disconnected fibers or chunks of material. They are being ejected by thermal, mechanical shear, and buildup of inner pressure stresses. They could also be produced by soot formation, a by-product of the pyrolysis process. Figure 1.4 illustrates the PICA-X sample ejecting particles in an arc-jet test.

Although the spalled particles carry away some heat, their presence shows adverse effect on surface heating. Since the ejection of the particles takes place before the material ablates, it causes an escalation in the heating rates at the surface and accelerates the material recession. The impact of ejection might create mechanical defects in the material, and an irregular surface leading to varying surface roughness. The boundary-layer flow over the
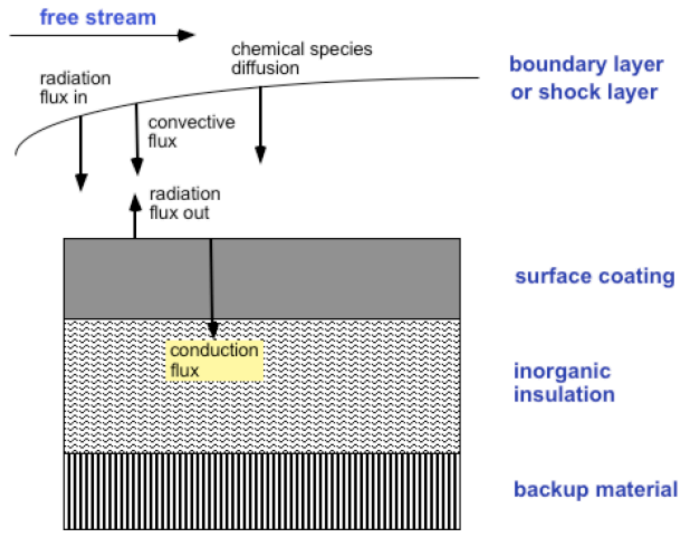
(a) Energy Accommodation of Non-Ablative TPS material
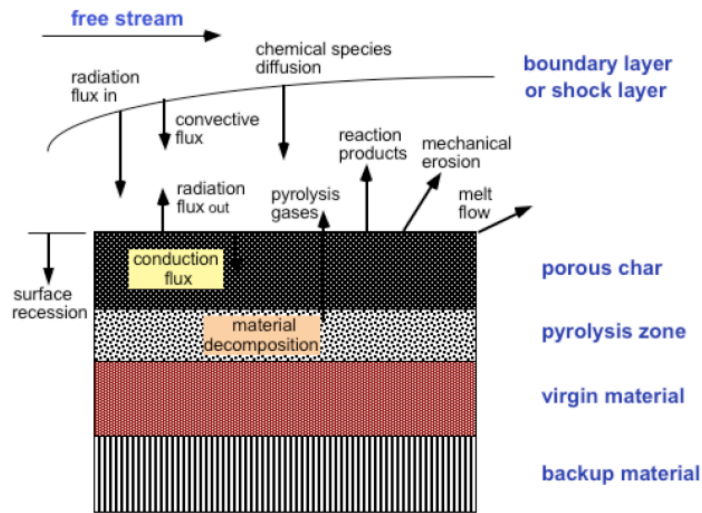
(b) Energy Accommodation of Ablative TPS material

Figure 1.3: Behavior of TPS materials

(Images taken from Ref. [27])
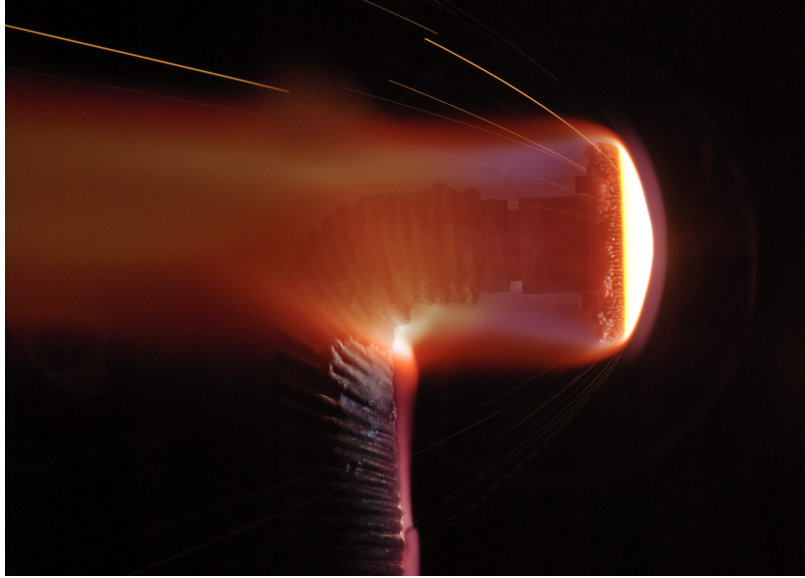
Figure 1.4: Arc-Jet test on PICA-X material displaying spallation
(Courtesy of NASA [31])

roughened surface can trigger transition to turbulence in the flow. Furthermore, the relative motion of the particles to the flow creates eddies leading to additional turbulence. These turbulence effects tend to increase the surface heating rates. The particles flow through high-temperature regions and thus radiate energy back to the surface as they tend to get heated up, thereby increasing the heat flux. Along their path, they tend to react chemically and physically with species in the flow. This changes the chemical composition of the flow field, thereby altering the aerodynamic heat rates, and hence modifying the radiative heat flux.

Past experiments conducted by Lundell and Dickey [32] on ATJ Graphite, by Brewer [33] and by Kratsch, Loomis and Randles [34] on carbon-phenolic recognized spallation as the reason for discrepancies between theoretical and experimental values. When experiments were conducted on ablative heat shields of Pioneer-Venus [35] and Galileo Probes [36, 37, 38], disagreements were found when the measured heating/ablating rates and temperature profiles

were compared with the theoretical analysis. The rates were over-predicted at the stagnation point and under-predicted in the downstream region. The results suggested that there were additional mechanisms that caused an increase in heat rates in the downstream region, and one possible mechanism among them was spallation. Furthermore, when spectroscopic measurements were performed by Raiche and Driver [39] at the NASA Ames Research Center to observe the effect on emission spectra while ablation occurs, the results were unexpected. The measurements of radiation intensity emitted by the shock layer taken from the side view position over a range of wavelengths of 400 nm to 900 nm found a continuum radiation ahead of the shock wave. The radiation corresponded to a black body at about 3800 K, and was likely due to the presence of spalled particles. Also, when spectroscopic measurements were performed by Kihara et. al. [40], the presence of C emission spectra in the argon arc-jet case, and the presence of CN emission spectra in the nitrogen and air arc-jet cases were detected in the upstream region of the shock. Similarly, spectroscopic measurements performed by Yoshinaka et. al. [41] in an air arc heated wind tunnel around a flat disk have demonstrated the presence of CN emission spectra as one of the strongest in the inviscid region. The reason for the C and CN emission spectra in the inviscid region, from the above mentioned spectroscopic measurements, is likely due to the presence of carbonaceous spalled particles; only particles could reach a region ahead of the shock.

1.3   Past Research on Spallation

A limited amount of research has been performed on spallation phenomenon. This is in sharp contrast with the amount of research devoted to other ablation mechanisms.

Various studies were conducted to determine the cause of spallation. These were based on the principle that when the combined thermal and mechanical stresses equal or exceed the ultimate stress of char, and the char layer was removed when its thickness reaches a critical value. Dhanak [42] performed a dimensional analysis and combined with the simple boundary

layer flow to determine the surface recession effect. Also, Scala and Gilbert [43] performed a quasi-steady state analysis of mechanical spallation. Further studies were performed by Robbins [44] on various ablative materials to investigate comparative mechanical spallation at different environmental conditions. Based on these studies, Acurex Corporation [45] implemented an empirical parameter to account for mechanical spallation and incorporated in Charring Materials Ablation (CMA) code. Later, Mathieu [46] included the spallation model responsible for char removal in the transient ablation analysis of charring ablators exposed to re-entry heating conditions. He developed an empirical equation relating critical char thickness and shear stress, and added an equation relating normal stress and pressure drop to evaluate the spallation effects on transient ablation. Furthermore, Schneider et. al. [47] analyzed the transient thermal/structural response of carbon phenolic ablator in ballastic re-entry and hyper-thermal ground tests environments. Their study concluded that the char removal by spallation accounted for two-thirds of total surface recession.

Dunbar et. al. [48] studied the interaction of spalled particles in the flow field which resulted in the increase of heat transfer rates (also called heating augmentation). It was concluded that the increase in convective heating was due to particle distortions. The transfer of kinetic energy of particles to thermal energy also resulted in heating augmentation. With this analysis, they developed an empirical relationship between stagnation region heat transfer and particles. Similarly, Holden et. al. [49] studied the correlation between heating augmentation and particle trajectories. It was found that the increase in heating rates was minimal when particles travel without penetrating the shock, and were increased by 3 to 10 times when particles penetrate through the shock.

In order to evaluate the spallation mass loss from an ablative material, laser irradiation tests [50, 51], ballistic-range tests [52, 53, 54] and arc-jet tests [55] were conducted. The main aim of the tests was to study the ablative mechanism behavior and validate the numerical codes based on the experimental results. Lundell and Dickey [50] performed experiments

on ATJ Graphite, carbon phenolic and Carbitrex 100 (carbon-carbon composite) exposed to intense laser radiation [56] and compared the heat of ablation values with a simple thermochemical ablation theoretical values. It was observed that for ATJ Graphite and carbon phenolic materials, the experimental values were less than the theoretical ones, and spallation was the reason for the discrepancies. Also, it was noticed that spallation was effective in blocking the beam energy and the effectiveness increased with the laser intensity. Later, Lundell [51] experimentally investigated the spallation mass loss on carbon phenolic composites used for Galileo probe forebody heat shield. A special particle canister [57] was designed in which test specimens of Chopped-Molded carbon phenolic (CMCP) and Tape-Wrapped carbon phenolic (TWCP) composites were mounted, and was coupled to a gas dynamic laser [56]. The spalled particles were captured in the canister and weighed to evaluate the spallation mass loss. Figure 1.5 illustrates the specially designed canister used in the experiment. The steady state spallation rates recorded at different laser intensities were correlated to the Galileo probe flight conditions. It was observed that spallation constituted 7.4% of expected thermochemical mass loss for nominal Jovian atmosphere, and 10% of expected thermochemical mass loss for cold-dense Jovian atmosphere.

Park et. al. [55] conducted tests on a carbon phenolic blunt body in a hydrogen-helium arc-jet wind tunnel at Galileo probe heating conditions. The recorded values were compared with the theoretical values given by Radiating Shock Layer Environment (RASLE) [58] and CMA [59] codes, and it was noticed that the former values were greater than the latter ones which were believed to be due to spallation. It was also found that spallation rate was about 15% and 30% of total ablation rate for wall heat fluxes of about 20 kW/cm^2 and 30 kW/cm^2.

Ballistic-range tests were conducted on carbon phenolic and carbon-carbon flat disks in argon environment by Park [52, 53]. It was revealed that the difference between the test and theoretical values, 60% for carbon phenolic and 30% for carbon-carbon, was attributed to spallation. Also, it was seen that the spallation in carbon phenolic was twice more than

for carbon-carbon, and was nearly thrice more than the spallation found by laser tests. The spalled particles were very small in case of carbon-carbon whereas in the case of carbon phenolic, they were ranging from very small to very large. The luminosity of spalled particles was found to be relatively constant for the carbon-carbon model and irregular for the carbon phenolic model. With only 5% of the total volume of the carbon phenolic model prone to indentations due to spallation of large particles, it was concluded through tests that only one-tenth of the total spallation was due to large particles. Later, Park and Balakrishnan [54] conducted ballistic range tests in argon atmosphere on carbon phenolic materials used for the Galileo Probe and it was found that the spallation rate was on the order of 10% of the total ablation rate.
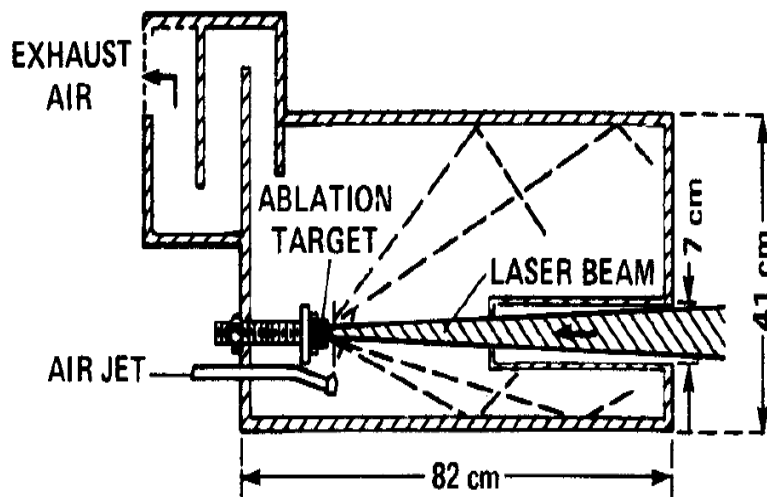
Figure 1.5: Specially-designed Canister used to collect the spalled particles (Courtesy of NASA [51])

Sullivan and Kobayashi [60] updated the CMA code by adding the spallation phenomenon. Thermal and mechanical stresses, which are responsible for particle ejection, were calculated for carbon phenolic annular cylinder and Kevlar Epoxy flat plate geome-

tries. Also, surface recessions were calculated using the code and compared with the test values [47, 61]. It was observed that by varying the Poisson's ratio and the thickness for cylinder and plate respectively, the predicted values can be matched with the test results.

In the early 70's, analytical methods for particle removal were developed by Ziering et. al. [62], Dolton et. al. [63], and McVey et. al. [64]. They used experimental data to empirically fit the parameters used in their equations. Later in the mid 90's, Ren et. al. [65] developed an analytical theory for the mechanical erosion of ablative materials where the parameters in the equations were independent of tests. The analytical method was validated by comparing with the experimental data which showed agreement.

On numerical side, Davies and Park [66] developed a solution technique to compute the trajectories of spalled particles with vaporizing mass. The numerical code was coupled with the Galileo Probe flow field solution computed by a Computational Fluid Dynamics (CFD) code, COLTS [67]. The experimental results from the laser irradiation ablation test [68] were considered to predict a set of initial particle sizes and ejection velocities. This set of parameters was used as input to study the behavior of spalled particles. It was found that a supersonic flow field surrounded the particle throughout its travel due to a significant slip between the flow field and the particle. The results also concluded that a substantial fraction of particle mass was vaporized, especially ahead of the shock.

Later, Park [69] developed a numerical model by implementing initial mass and velocity of the particle as Gaussian functions. By assuming the parameters to be constant values and integrals of equation of motion as a polynomial expansion, computations of trajectories, production rates, and turbulence energy were performed at all points on the ablator surface for all ranges of mass and velocities. It was observed that the production rates decay exponentially in the normal direction. Expressing maximum values and slopes of decay of these rates as a function of characteristic particle size, velocity, and ambient atmospheric density, and comparing the rates with the spectroscopic results of the carbon-phenolic model ablating in

13

an arc-jet wind tunnel, it was recommended that the lower limits of size and velocity of the spalled particle were of order 10 μm and 100 m/s. Park continued to apply this numerical method to find the radiant energy/flux [70] due to the spalled particles based on optical measurements conducted by Raiche and Driver [39]. Particle size and velocity was assumed to be a function of mass and was varied to compute the parameters. When compared with the experimental evidence, it was found that the spalled particles contributed 170 W/cm^2 radiative heat flux and when correlated with stardust re-entry mission heating conditions, spalled particles yielded up to 8% of total heat flux at the stagnation point. Based on the same experiment, Pace et. al. [71] developed a spallation model for constant mass particles using a Eulerian frame of reference to evaluate the impact of them on radiative heating. The model treated the particles as a continuum material, and the model was integrated to the CFD code DPLR [72]. Additional calculations were performed to compute the radiative intensity using NEQAIR [73].

At Kyushu University, Kihara et. al. [40] conducted ablation experiments on carbon phenolic material in an arc-jet of argon, air, and nitrogen environments. Spectroscopic measurements were conducted at places upstream and downstream of the shock wave. During those tests, CN spectra and a line spectrum of C behind the shock layer in air and nitrogen environments were observed, whereas only C spectrum in argon environment was seen. Ahead of the shock layer, CN and C_2-swan spectra was observed. Figure 1.6 shows the emission spectra of CN and C_2 as found in measurements. It was proposed that the traces of CN upstream of the shock were produced when the carbon vapor from the particle reacted with the nitrogen in the flow field. A numerical model was also developed to analyze the particles penetrating the shock not be sublimated out inside the shock layer. Later, Nozawa et. al. [74] developed a model for simulation of a particle's trajectory which included its sublimation behavior. The above experiment was used as evidence and emphasis was made on particles penetrating the shock. The particle size was limited between 20 μm and

100 µm by taking into account results from the Park model [69] and experimental results. The investigation of the numerical model for some combinations of initial conditions showed that some trajectories were close to the experimental ones. It was seen that small particles (less than 20 µm) needed very high initial velocity to penetrate the shock and sublimation energy was ineffective for heat balance of the particle.
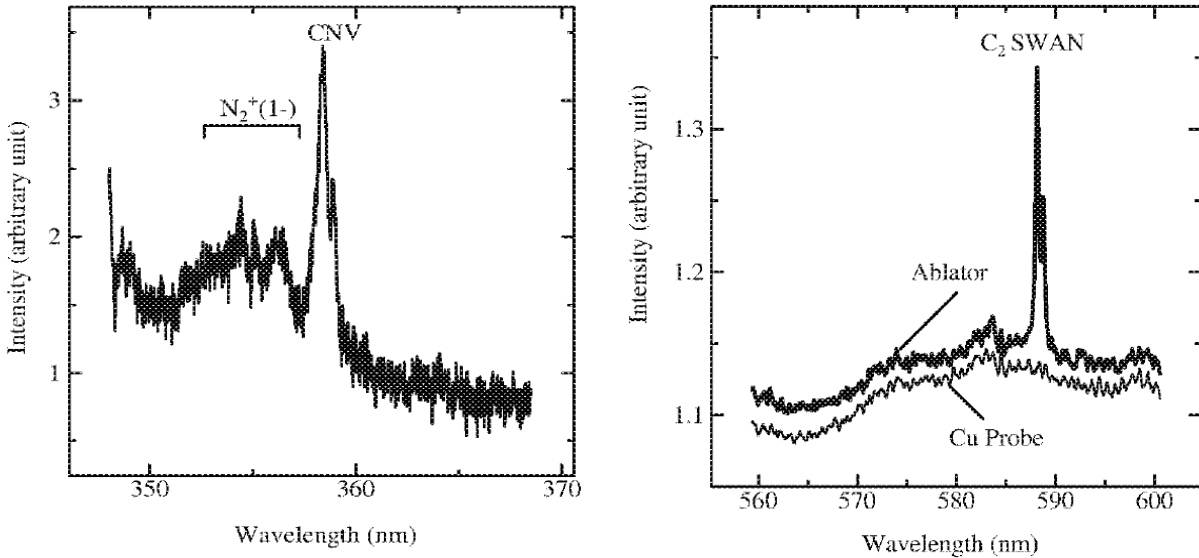
(a) CN spectra observed upstream of the shock   (b) C_2 Swan spectra observed upstream of the shock

Figure 1.6: Spectroscopic Results

(Reproduced with permission of JSASS, Transaction of the Japan Society for Aeronautical and Space Sciences, vol.49, no.164, pp.65-70, 2006. Copyright remains with JSASS © [40])

For designing the TPS for space missions to Mars, experiments were conducted by Esser et. al. [75, 76] in Martian atmospheric conditions comprising of dust particles on ablative material. The tests were done on Norcoat Liège material in an arc-jet facility to study the impact of these dust particles on ablation phenomena during the re-entry. Initially, the ablative material was tested at different conditions in flow without dust particles (called the reference test), and later tested at same conditions in dust loaded flow. Boron Nitride (BN) particles were used as the baseline dust particles and tests were performed for different sizes

of particles. Mass loss and surface degradation were measured, and the results depicted that these values were higher in dust erosion tests. Also, surface temperature of the material was lower in dust erosion tests than in reference tests. It was speculated that the top layer of char was removed by the impinging dust particles, leading to colder material from below to exposure and thus, resulting in a lower surface temperature. Figure 1.7 (a) demonstrates the dust-loaded flow over the ablative sample and exhibiting spallation.

Recently, MacDonald et. al. [77] conducted experiments on the ablative materials Asterm and Carbon Bonded Carbon Fiber (CBCF), in a subsonic air plasma flow at a temperature of approximately 6000 K. It was noticed that for the CBCF sample, spallation was observed at a test condition (surface temperature of 1430 K, ratio of radially to swirling injected air of 4:5) whereas no spallation and cooler boundary layer region were observed encompassing the boundary layer at another test condition (surface temperature of 1750 K, ratio of radially to swirling injected air of 3:1). Similarly, no spallation and sodium emission along with colder boundary layer region was found for the Asterm sample at a similar test condition (surface temperature of 1740 K). Figure 1.7 (b) shows the extreme spallation behavior by CBCF in this experiment.

In order to employ accurate safety margins for designing the heat shields, there is a need for a more explicit understanding of the spallation phenomenon. Using experimental techniques to study the behavior of a single spalled particle and its impact on the flow field is a difficult task. However, numerical model validated by empirical evidence can be used to evaluate the importance of the spallation phenomenon. Although various numerical models were developed in the past as listed above, the chemical behavior of particles was not given enough importance. The source of emission spectra manifested by spectroscopic measurements was believed, by a few researchers, to be only due to the sublimation of spalled particles. In contrast, the particles traversing through a weakly ionized flow field tend to react with chemical species leaving behind traces of products in the shock layer. Hence,
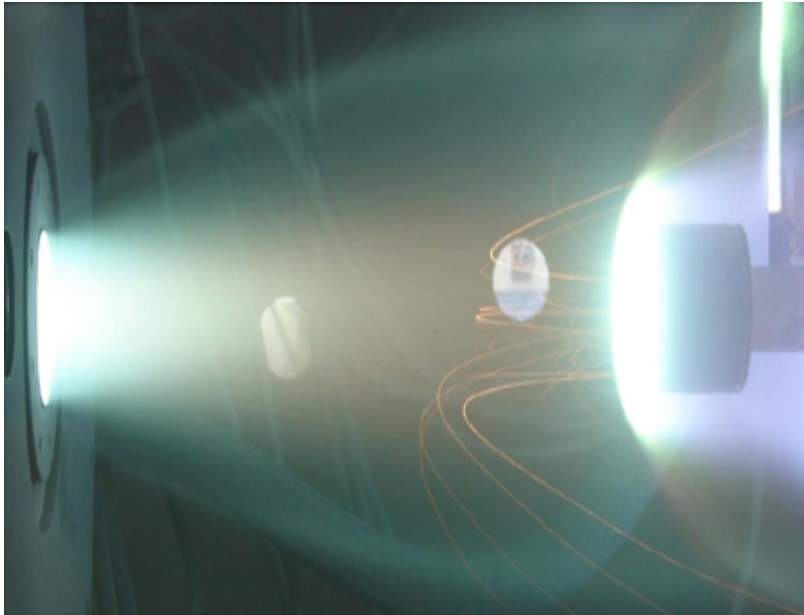
(a) Dust erosion test in DLR H2K wind tunnel
(Copyright © CNES, HPS, DLR [78])
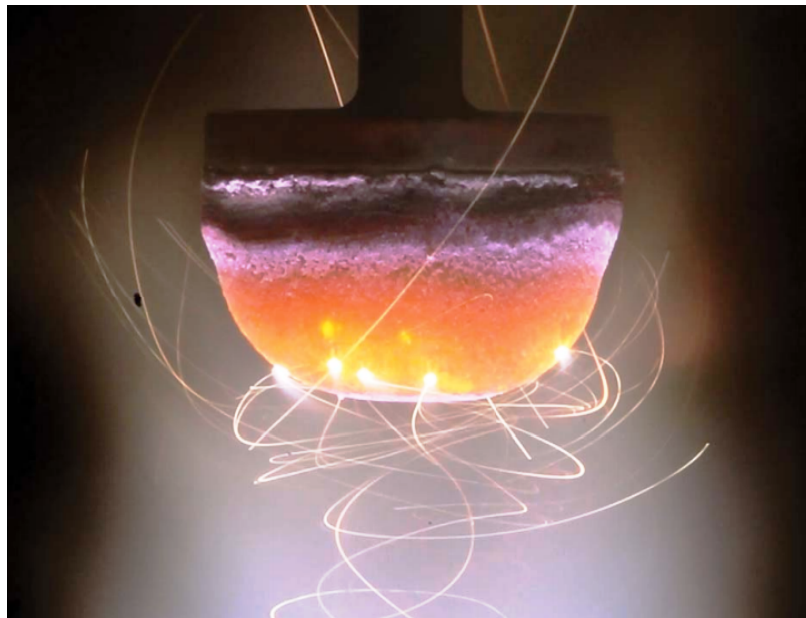
(b) Subsonic Air Plasma flow at 6000°K on CBCF
(Copyright © 2014 IEEE [77])

Figure 1.7: Arc-jet tests on different ablative material exhibiting spallation

it is necessary to also consider the surface chemical reactions of the particle, along with sublimation, to evaluate the significance of the spallation phenomenon.

In the present work, a particle-tracking code to compute the properties and trajectories of the spalled particles as they are ejected from the surface is developed. The code also accounts for the chemical interactions of the particles, and tracks the carbon trail as the particle travels through the flow field. In order to do so, the spallation model is one-way coupled to the CFD module [79] of the Kentucky Aerodynamic and Thermal-response Solver (KATS) to obtain the flow field parameters. The code is verified, to confirm correctness of the numerical code and order of accuracy of discretization, using the Method of Manufactured Solutions (MMS). The results from the code could be used to quantify the effect of spalled particles on various ablative surfaces. Later, the spallation code is loosely coupled with KATS CFD code to analyze the effects of spalled particles on flow field.

Chapter 2 Mathematical Formulation of the Spallation code

The code computes the properties of the particle as it traverses through the flow field by solving the mass, momentum and energy equations. A chemistry model is included to account for the surface reactions occurring on the particle's surface, along with its vaporizing behavior. The assumptions, the general formulation of the governing equation, and the derivation of mass, momentum, and energy conservation equations are thoroughly discussed in this chapter.

2.1   Basic Assumptions

In order to simplify the approach, the following assumptions are considered:

1. The particle is a graphite sphere.

2. Heat and mass transfer around the surface of the particle are assumed to be uniform. Uniform mass transfer is assumed to preserve the spherical shape of the particle throughout its travel.

3. The distribution of temperature inside the particle is considered uniform.

4. Physical properties of the particle are assumed to be constant.

5. The rotational motion of the particle is neglected and is assumed to have only translational motion.

6. The local shock formed in front of the particle when the relative velocity with the flow crosses subsonic range [80] is neglected.

2.2 Governing Equations

A lagrangian frame of reference is employed to compute the path of the spalled particle. The governing equations are thus in the form of:

$$\frac{D\mathbf{U}}{Dt} = \frac{\partial \mathbf{U}}{\partial t} = \mathbf{W} \tag{2.1}$$

where $\mathbf{U}$ is the state vector and $\mathbf{W}$ is the source vector matrix. The elements of the state vector $\mathbf{U}$, which denote the conserved variables are :

$$\mathbf{U} = \begin{pmatrix} m_p \\ m_p u_p \\ m_p v_p \\ m_p w_p \\ m_p E_p \end{pmatrix} \tag{2.2}$$

where m_p is the mass of the particle, (u_p, v_p, w_p) are the velocity components of the particle, and E_p is the total energy of the particle.

2.3 Equation of motion

The motion of the particle is dictated by the force acting on it. It is assumed that the important force acting on the particle is drag force generated by the flow field. Magnus force, Basset force, added mass, and other external forces like gravitational and buoyancy forces are not taken into account. Hence, the particle's motion in the x-direction is given by:

$$\frac{\partial}{\partial t} (m_p u_p) = F_{D_X} = \frac{1}{2} C_D \rho_f A_p (u_f - u_p) V_r \tag{2.3}$$

where F_{D_X} is drag force in the x-direction, C_D is the drag coefficient, ρ_f is the density of the flow field, A_p is the cross-sectional area of the particle, u_f is the velocity of the flow field in the x-direction, and V_r is the relative velocity between the particle and flow field. Similar equations are applied to the other two directions.

Coefficient of Drag

The spalled particles are of the order of microns, and are comparable to the fluid flows mean free path. Hence, the drag coefficient should take into account the rarefaction effects. The Henderson model [81] is considered in this work to evaluate coefficient of drag C_D used in Eq. 2.3. This model is valid for Mach numbers up to 6 and for flows ranging from continuum to free molecular flows including slip and transition flows. The Henderson model equation also includes the effect of particle and flow field temperatures on the drag coefficient.

$$
C_D = \begin{cases}
\left\{ 24 \left[\text{Re} + S \left\{ 4.33 + \dfrac{3.65 - 1.53 \left(\frac{T_p}{T_f}\right)}{1 + 0.353 \left(\frac{T_p}{T_f}\right)} \exp\left(-0.247 \frac{\text{Re}}{S}\right) \right\} \right]^{-1} \right. \\
\left. + \exp\left(-\frac{0.5M}{\sqrt{\text{Re}}}\right) \left[\dfrac{4.5 + 0.38 \left(0.03\text{Re} + 0.48\sqrt{\text{Re}}\right)}{1 + 0.03\text{Re} + 0.48\sqrt{\text{Re}}} + 0.1M^2 + 0.2M^8 \right] \right. & \text{if } M \leq 1 \\
\left. + 0.6S \left[1 - \exp\left(-\frac{M}{\text{Re}}\right)\right] \right\} \\[2em]
C_{D_{(M=1)}} + \frac{4}{3}(M-1)\left(C_{D_{(M=1.75)}} - C_{D_{(M=1)}}\right), & \text{if } 1 < M \leq 1.75 \\[2em]
\dfrac{0.9 + \left(\frac{0.34}{M^2}\right) + 1.86\left(\frac{M}{\text{Re}}\right)^{\frac{1}{2}} \left[2 + \frac{2}{S^2} + \frac{1.058}{S}\left(\frac{T_p}{T_f}\right)^{\frac{1}{2}} - \frac{1}{S^4}\right]}{1 + 1.86\left(\frac{M}{\text{Re}}\right)^{\frac{1}{2}}}, & \text{if } M > 1.75
\end{cases}
$$

$$(2.4)$$

where M is Mach number, Re is Reynolds number, and S is the molecular speed ratio which is calculated as:

$$
S = M\sqrt{\frac{\gamma}{2}} \tag{2.5}
$$

where γ is the ratio of specific heats. The diameter of the particle (d_p) and relative velocity (V_r) are used as length and velocity scales to calculate Reynolds number. Similarly, Mach

number is calculated based on relative velocity. The dynamic viscosity (μ) used in the formulation of Reynolds number is calculated from Wilke's semi-empirical mixing rule [82] where Blottner's curve fits [83] are used to calculate the individual species viscosities.

2.4 Heat balance of the particle

The total energy of the particle is the sum of internal energy and kinetic energy, which are due to its surface temperature and motion, respectively. The energy is dissipated in the form of power drag, radiative heat rate, convective heat rate, and rate of heat produced due to surface reactions. It can be formulated as:

$$\frac{\partial}{\partial t}\left(m_p E_p\right) = \frac{\partial}{\partial t}\left(m_p C_{v_p} T_p + \frac{1}{2}m_p\left(u_p^2 + v_p^2 + w_p^2\right)\right) = \dot{q}_{conv} + p_{drag} - \dot{q}_{rad} + \dot{q}_{rxn} \qquad (2.6)$$

where C_{v_p} is the specific heat capacity at constant volume of the particle, T_p is the particle's temperature, $\dot{q}_{conv}$ is the convective heat rate transferred, p_{drag} is the power drag, $\dot{q}_{rad}$ is the radiative heat rate, and $\dot{q}_{rxn}$ is the heat rate produced by the surface reactions of the particle.

It is important to note that the internal energy E_T of the particle is given by:

$$E_T = \int C_{v_p} dT = \int_{T_{ref}}^{T_p} C_{v_p} dT + \Delta H_f^{\circ} \qquad (2.7)$$

where ΔH_f° is standard enthalpy of formation. In the case of carbon (graphite), $\Delta H_f^{\circ} = 0$. The reference temperature T_{ref} is considered to be 0 K. Also, as the specific heat capacity is assumed to be constant (as indicated in Assumption 4), the internal energy E_T can be expressed as:

$$E_T = C_{v_p} \int_0^{T_p} dT = C_{v_p} T_p \qquad (2.8)$$

Power Drag

As the drag force is the only force acting on the particle that dictates its path, the work done by this force is represented by the power drag (p_{drag}). Power drag is the power required by the particle to overcome the resistance (drag force) produced by the flow field and is given as:

$$p_{drag} = \frac{1}{2} C_D \rho_f A_p V_r^3 \tag{2.9}$$

Power drag plays a vital role in the path of the particle. The small size of the particle results in a high drag coefficient, and hence it experiences a high resistance to overcome. In overcoming such high resistance, the particle loses its energy in terms of heat thereby acquiring high surface temperatures.

Radiative heat rate

Only radiative emission (also called radiation cooling) from the particle is considered here and radiative absorption of the particle is neglected. The heat rate in the form of radiation from the particle is calculated using the Stefan-Boltzmann law integrated over the surface of the particle.

$$\dot{q}_{rad} = \epsilon \sigma T_p^4 A_s \tag{2.10}$$

where ϵ is the emissivity of the particle, σ is the Stefan-Boltzmann constant, and A_s is the surface area of the particle.

Convective heat rate

The heat transfer between the particle and the flow field takes place in the form of convective heat and its rate is given as:

$$\dot{q}_{conv} = \text{Nu}\frac{[\kappa_{tr}\left(T_{f_{tr}} - T_p\right) + \kappa_{ve}\left(T_{f_{ve}} - T_p\right)]}{d_p}A_s \tag{2.11}$$

where Nu is the Nusselt number, κ is the fluid thermal conductivity, T_f is the fluid temperature, and subscripts tr and ve denote translational-rotational energy mode and vibrational-electronic energy mode, respectively. The thermal conductivity of the flow field is calculated using Wilke's semi-empirical mixing rule [82] where Eucken's relation [84] is used to calculate individual species thermal conductivities present in the flow field.

Nusselt number

The Nusselt number Nu used in Eq. 2.11 is derived from the Carlson and Hoglund model [85]. This model includes the rarefaction effect and is given as:

$$\text{Nu} = \frac{2 + 0.459\text{Re}^{0.55}}{1 + 3.42\frac{\text{M}}{\text{Re}}\left(2 + 0.459\text{Re}^{0.55}\right)} \tag{2.12}$$

Heat rate due to surface reactions

The particle undergoes oxidation and nitridation when its surface reacts with O, O_2, and N species in the flow field. Additionally, the increase in the surface temperature of the particle along its path contributes to sublimation. The chemical reactions are discussed in Section 2.5. The heat rate due to these reactions can be expressed as:

$$\dot{q}_{rxn} = \dot{q}_{\text{O}} + \dot{q}_{\text{N}} - \dot{q}_{\text{O}_2} - \dot{q}_{sub} \tag{2.13}$$

where $\dot{q}_{\text{O}}$, $\dot{q}_{\text{O}_2}$, and $\dot{q}_{\text{N}}$ are the heat rates produced by oxidation and nitridation of the particle with atomic oxygen (O), molecular oxygen (O_2), and atomic nitrogen (N) respectively. As for $\dot{q}_{sub}$, it is the heat rate produced by the sublimation of the particle.

The heat rates due to chemical reactions on the surface of the particle [86] are computed as:

$$\dot{q}_i = A_s \left(|\Delta h_i| \frac{\bar{\nu}_i c_i}{4} \right) \quad \text{where} \quad i = \text{O, O}_2\text{, N} \tag{2.14}$$

where Δh_i is the enthalpy of a reaction involving species i, c_i is the concentration of species i at the particle's surface, and $\bar{\nu}_i$ is the mean thermal speed of the species i. The constant values of Δh for the reactions are taken from Refs. [86, 69]. The mean thermal speed of the species is calculated as:

$$\bar{\nu}_i = \sqrt{\frac{8RT_f}{\pi M_{wi}}} \tag{2.15}$$

where T_f is the flow field temperature and M_{wi} is the molecular weight of the species i. Since the CFD code uses a two-temperatures model to account for thermal non-equilibrium in the flow field, only translational temperature is considered in Eq. 2.15.

The heat rate produced by sublimation is given by:

$$\dot{q}_{sub} = A_s \left(\sum \Delta G_{f_i} J_i \right) \quad \text{where} \quad i = \text{C}_1\text{, C}_2\text{, C}_3 \tag{2.16}$$

where ΔG_{f_i} is the Gibbs free energy of formation, and J_i is the vapor flux of C_i species formed. Standard Gibbs free energy of formation $(\Delta G_{f_i}^{\circ})$ is interpolated from the JANAF tables [87] at the temperature of the particle, and ΔG_{f_i} is calculated at the pressure of the C_i vapor (P_{C_i}) whose formulation is given as:

$$\Delta G_{f_i} = \Delta G_{f_i}^{\circ} + R\, T_p \ln \frac{P_{\text{C}_i}}{P_{\text{C}_i^{\circ}}} \tag{2.17}$$

where $P_{\text{C}_i}^{\circ}$ is the atmospheric pressure and R is the universal gas constant. The vapor flux J_i and vapor pressure P_{C_i} are calculated using Eq. 2.21 and Eq. 2.22.

25

2.5 Particle surface reactions

The species present in the flow field react with the particle by impinging on its surface and forming the chemical products. The individual atoms and molecules of the species are in random motions and chemically react by colliding with the particle, which is also in motion too. However, the speed at which collision takes place ensures direct formation of products without any adsorption/desorption steps. Hence, the adsorption mechanism is not considered. The possible reactions occurring on the surface of the particle, as mentioned earlier, are oxidation, nitridation, and sublimation.

Oxidation

The oxidation by atomic and molecular oxygen at the surface of the spalled particle are given by the irreversible reactions:

$$C(s) + O \longrightarrow CO$$
$$2\,C(s) + O_2 \longrightarrow 2\,CO$$
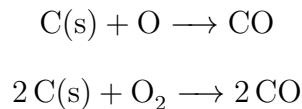
The oxidation by atomic oxygen lead to an exothermic reaction, whereas molecular oxygen lead to an endothermic reaction.

Nitridation

The nitridation by atomic nitrogen at the particle's surface is given by the irreversible reaction:

$$C(s) + N \longrightarrow CN$$

The above equation is an exothermic reaction by nature.

Sublimation

Sublimation is a function of the temperature of the particle. The amount of vapor formed due to sublimation is solely based on its surface temperature. For sublimation, the following irreversible endothermic reactions are considered:

$$C(s) \longrightarrow C(g)$$

$$2\,C(s) \longrightarrow C_2(g)$$

$$3\,C(s) \longrightarrow C_3(g)$$
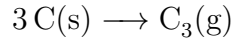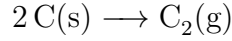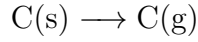
These chemical products are dominant among all the possible products and hence, this numerical model takes into consideration the above reactions as sublimative behavior of the particle.

Mass recession rate

The rate of mass recession of the particle due to oxidation and nitridation are calculated as:

$$\dot{m}_{C/CO} = M_{wC} \left(k_{f(O)}c_O + k_{f(O_2)}c_{O_2} \right) A_s \tag{2.18}$$

$$\dot{m}_{C/CN} = M_{wC} \left(k_{f(N)}c_N \right) A_s \tag{2.19}$$

where M_{wC} is the molecular weight of carbon, and $k_{f(i)}$ ($i = O, O_2, N$) is the forward reaction rate for a reaction involving species i. The forward reaction rate for three reactions can be expressed as:

$$k_{f(i)} = \frac{\gamma_{0(i)}}{4} \left[\bar{\nu}_i + V_r \right] \exp\left(-\frac{E_{R(i)}}{RT_p} \right) \quad \text{where} \quad i = O, O_2, N \tag{2.20}$$

where $\bar{\nu}_i$ is the mean thermal speed of species i which is computed as given by Eq. 2.15, $\gamma_{0(i)}$ is the reaction efficiency and $E_{R(i)}$ is the energy barrier for reaction involving species i.

The mass of the particle receded due to the sublimation process is calculated using the Knudsen-Langmuir equation [88]:

$$\dot{m}_{C/sub} = \sum J_i A_s = \sum \alpha_{v_i} P_{C_i} \sqrt{\frac{M_{wi}}{2\pi R T_p}} A_s \quad \text{where} \quad i = C_1, C_2, C_3 \tag{2.21}$$

where α_{v_i} is the vaporization coefficient [89] of reaction producing species i and M_{wi} is the molecular weight of species i. The behavior of vapor flux as a function of temperature for C_1, C_2, and C_3 is illustrated in Figure 2.1. The vapor pressure P_{C_i} of species i is calculated using the Clausius-Clapeyron equation as given by Eq. 2.22, and the thermochemical data of constants are taken from Palmer and Shelef [90], which are given in Table 2.1.

$$\ln P_i = \frac{A}{T_p} + B \tag{2.22}$$
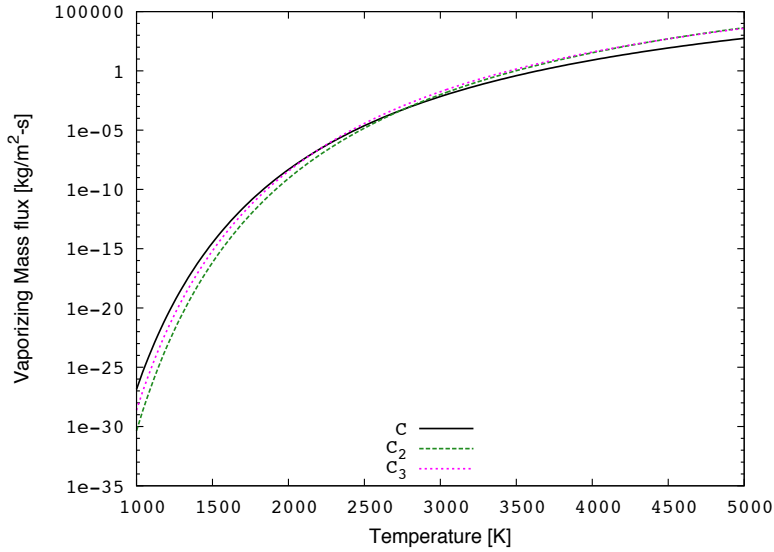
Figure 2.1: Behavior of vaporizing flux of carbon as a function of temperature

Table 2.1: Clausius-Clapeyron equation constants for C_1, C_2, C_3

Species	A	B
C_1	-85715	18.69
C_2	-98363	22.20
C_3	-93227	23.93

Chemistry model

The parameters $\gamma_{0(i)}$ and $E_{R(i)}$ used in Eq. 2.20 are taken from Driver et. al. [91, 92] and are listed in Table 2.2. Driver et. al. evaluated reaction efficiencies for oxidation reactions by performing experiments on Fiberform and PICA samples. In their study, sublimation was not considered since the temperature of the samples were lower than the sublimation temperature. However, since the particle travels through a very high temperature flow field, sublimation is considered in this model.

Table 2.2: Values of γ_0 and E_R for the following reactions according to Driver's surface chemistry model

Reactions	γ_0	E_R (kJ/mol)
$C(s) + O \longrightarrow CO$	0.90	0
$2\,C(s) + O_2 \longrightarrow 2\,CO$	0.01	0
$C(s) + N \longrightarrow CN$	0.005	0

The total mass recession of the spalled particles can therefore be expressed as:

$$\frac{\partial m_p}{\partial t} = \dot{m}_p = \dot{m}_{C/CO} + \dot{m}_{C/CN} + \dot{m}_{C/sub} \tag{2.23}$$

Hence, the system of equations can be expressed by inserting Eqs. 2.3, 2.6 and 2.23 into Eq. 2.2.

$$\frac{\partial}{\partial t}\begin{pmatrix} m_p \\ m_p u_p \\ m_p v_p \\ m_p w_p \\ m_p E_p \end{pmatrix} = \begin{pmatrix} -\dot{m}_{C/CO} - \dot{m}_{C/CN} - \dot{m}_{C/sub} \\ F_{D_X} \\ F_{D_Y} \\ F_{D_Z} \\ \dot{q}_{conv} + p_{drag} - \dot{q}_{rad} + \dot{q}_{rxn} \end{pmatrix} \qquad (2.24)$$

Chapter 3 Numerical modeling

3.1 Solution approach

Discretization of the system of equations in Eq. 2.24 is carried out using backward Euler method. The mass conservation equation is uncoupled from the momentum and energy conservation equations, and both sets of equations are solved using the Block Gauss-Seidel method. Initially, Newton's method is employed to solve momentum and energy equations. Among the computed output parameters, the temperature of the particle is inserted into the mass equation and solved again by Newton's method to obtain new diameter/mass of the particle. The new computed mass is re-inserted again in the momentum and energy equations to compute new values. This process is repeated until the relative error between the computed values of two successive iterations is lower than 10^{-6}.

The position of the particle is calculated by solving the following equation:

$$\frac{\partial}{\partial t}\begin{pmatrix} x_p \\ y_p \\ z_p \end{pmatrix} = \begin{pmatrix} u_p \\ v_p \\ w_p \end{pmatrix} \tag{3.1}$$

where (x_p, y_p, z_p) are components of position of the particle. Therefore, in order to compute the trajectory of the particle, Eq. 3.1 is included into the system represented in Eq. 2.24. Hence, the system of equations numerically solved is:

$$\frac{\partial}{\partial t} \begin{pmatrix} m_p \\ m_p u_p \\ m_p v_p \\ m_p w_p \\ m_p E_p \\ x_p \\ y_p \\ z_p \end{pmatrix} = \begin{pmatrix} -\dot{m}_{\text{C/CO}} - \dot{m}_{\text{C/CN}} - \dot{m}_{\text{C}/sub} \\ F_{D_x} \\ F_{D_y} \\ F_{D_z} \\ \dot{q}_{conv} + p_{drag} - \dot{q}_{rad} + \dot{q}_{rxn} \\ u_p \\ v_p \\ w_p \end{pmatrix} \tag{3.2}$$

This model is an initial value problem, and the parameters to be assigned are:

1. Radius of the particle

2. Ejection velocity

3. Ejection position

4. Ejection angle

5. Temperature of the particle

However, the initial temperature of the particle is assumed to be the temperature of the surface from which it gets ejected, which is dictated from the flow field data.

3.2 Verification

Method of Manufactured Solutions (MMS) [93] is employed to verify the developed code. Each variable in the elements of state vector matrix $\mathbf{U}$ is expressed by a smooth function, also called a manufactured solution. The source term is computed by applying the differential operator to the governing equations. The elements of $\mathbf{U}$ along with the computed source terms are implemented in the discretized equations of the code and solved numerically. The

error between the numerical and exact solutions are compared against the theoretical order of accuracy based on the discretization performed in the code. Since the backward Euler method is employed for the discretization, the theoretical order of accuracy is first order in time.

The manufactured solution considered for the variables in the model is an exponential function of the form:

$$\mathbf{U} = ae^{bt} + c \tag{3.3}$$

where a, b, c are constant parameters and t represents time. The values considered for the parameters are listed in Table 3.1.

Table 3.1: Parameter values for different variables used in the manufactured solution

Parameters	a	b	c
d_p	-1.0	0.05	2.0
T_p	10.0	0.5	1000.0
u_p	-1.0	1.0	0.0
v_p	5.0	0.5	0.0
w_p	-0.01	-1.0	0.0

Several numerical tests are conducted for different time step sizes and are compared with analytical solution. Figure 3.1 illustrates the L_2 norm and maximum norm errors between numerical and exact solutions for different time step sizes. The errors are observed to increase exponentially by a factor of 2, therefore retaining the first order accuracy in time. Hence, the developed code is free from mathematical (verification-related) errors [94].
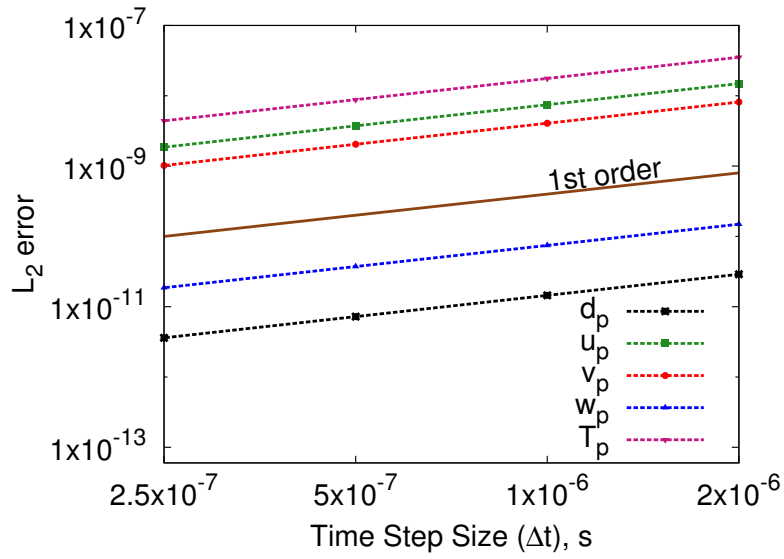
(a) L_2 norm error
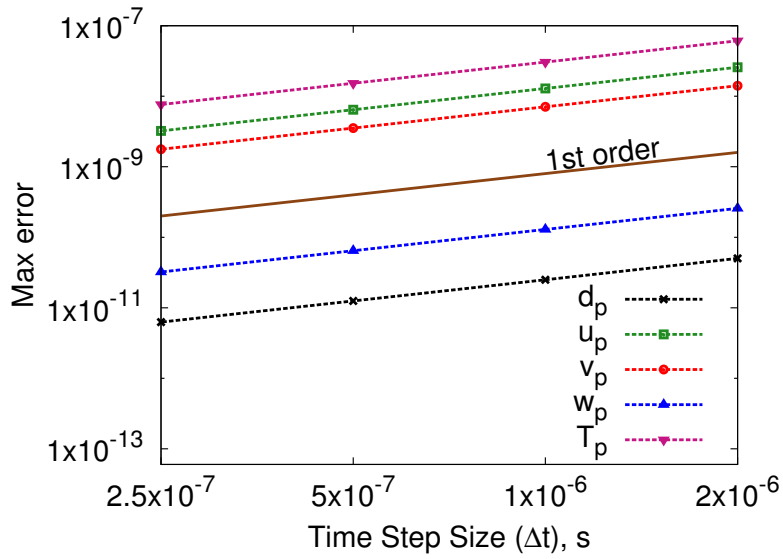
(b) Maximum norm error

Figure 3.1: Plots of L_2 norm error and maximum norm error

34

3.3 Flow Field

The flow field solutions used to calculate the trajectories of the particles are obtained using the hypersonic aerothermodynamic CFD code KATS. The test case considered here consists of Mach 5 high enthalpy flow over the sample. The geometry of the sample is presented in Figure 3.2.
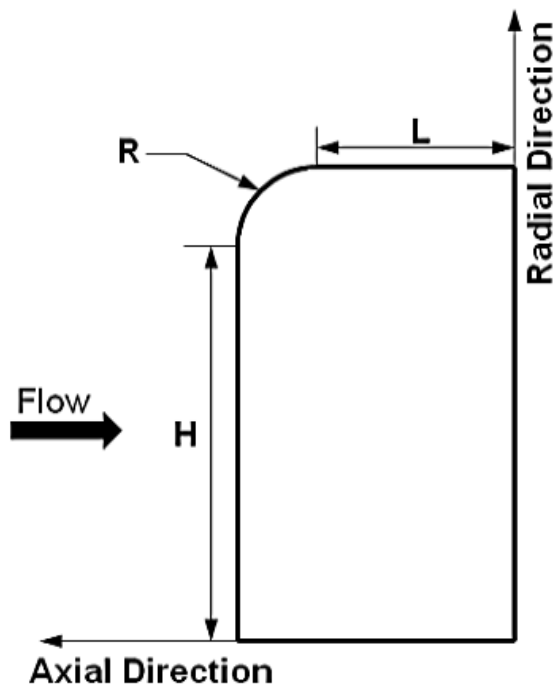
Figure 3.2: Schematic of the sample considered in the test cases: $H = 13.3$ mm, $R = 3.2$ mm and $L = 5$ mm

Two gases are considered: argon and air. The argon flow field is a non-reacting environment. Therefore, only the sublimation of the particle takes place. Since argon is a monoatomic molecule, no vibrational energy is present, and only translational temperature is computed. Figure 3.3 shows the flow field CFD solution of argon. The boundary conditions considered to generate this flow are given in Table 3.2 where ρ_f is the density of

the flow field, U_∞ is the free-stream velocity, and T_{tr}, T_{ve}, T_w are transitional-rotational energy mode temperature, vibrational-electronic energy mode temperature, wall temperature respectively.

Table 3.2: Boundary conditions of Mach 5 Argon flow

ρ_f	U_∞	T_{tr}	T_{ve}	T_w
kg/m^3	m/s	K	K	K
3.45×10^{-3}	3860	1470	1470	500

The air flow field consists of 6 species: Ar, N$_2$, O$_2$, NO, O and N. For this case, the particle undergoes oxidation and nitridation along with sublimation. Figure 3.4 demonstrates the CFD solution of air flow field. The free stream, wall boundary conditions, and species mass fractions considered to generate the flow field are given in Table 3.3 where Y_i is the mass fraction of species i ($= Ar, N_2, O_2, NO, N, O$).

Table 3.3: Boundary conditions and mass fractions of species for a Mach 5 Air flow

ρ_f	U_∞	T_{tr}	T_{ve}	T_w	Y_{Ar}	Y_{N_2}	Y_{O_2}	Y_{NO}	Y_N	Y_O
kg/m^3	m/s	K	K	K						
1.49×10^{-3}	3163	896	896	600	0.0704	0.7178	0.0613	0.0469	0.0000	0.1036

For the flow field solutions, a grid independence study was conducted on different grid resolutions, ranging from coarse to fine. A grid independent solution is chosen to be used in this work for each flow field environment.
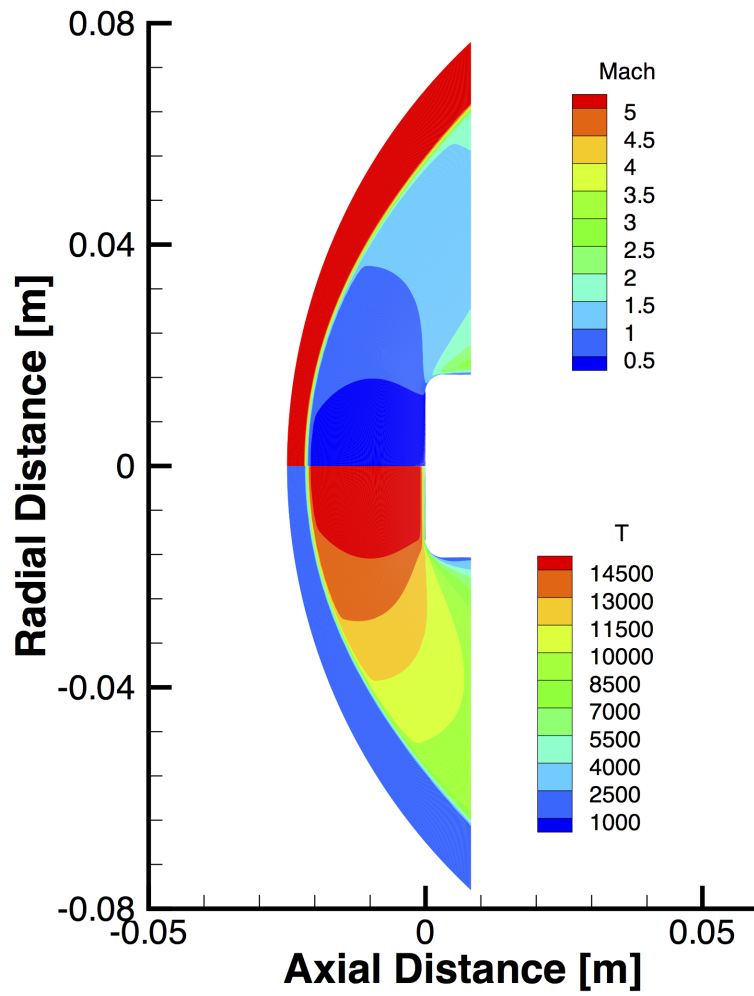
Figure 3.3: Mach 5 high enthalpy argon flow field around an ablative test piece
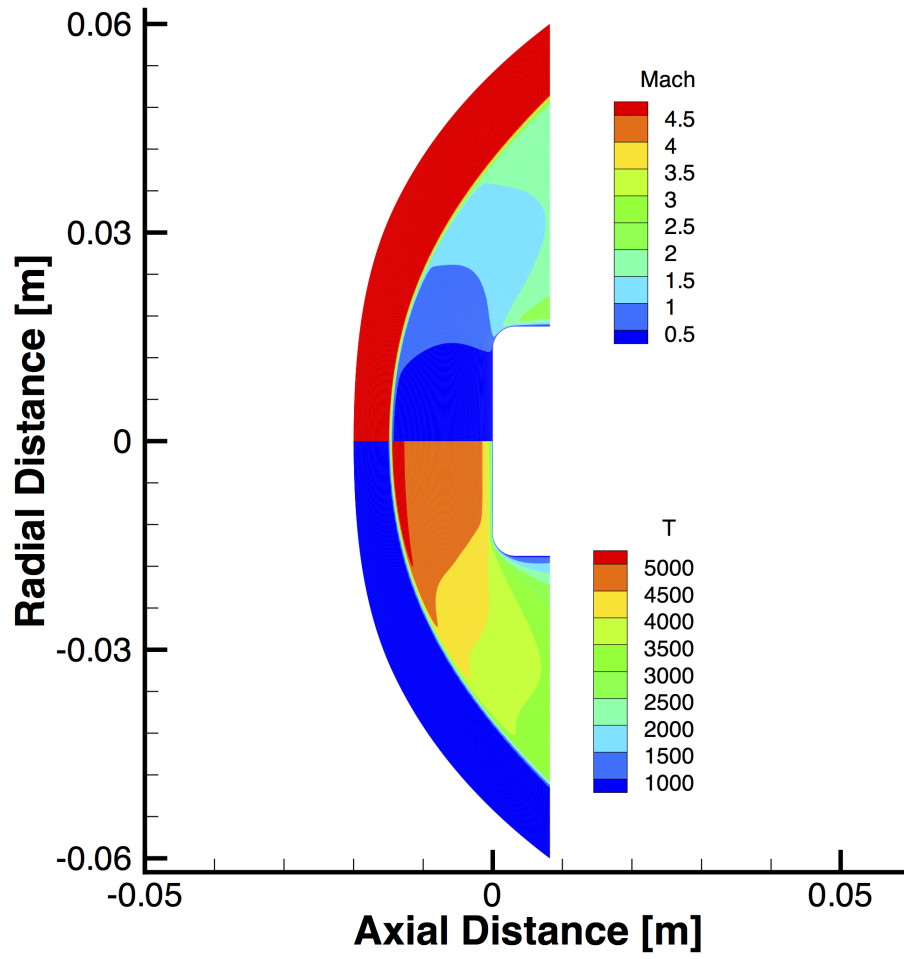
Figure 3.4: Mach 5 high enthalpy air flow field around an ablative test piece

Chapter 4 Results – One-way Coupling

The spectroscopic measurements performed at different locations in front of the sample, as discussed in Section 1.3, have detected the presence of spalled particles in the flow field. Though the measurements conducted behind the shock indicate the effects of ablative mechanisms, including spallation, those conducted ahead of the shock represent only the effects of spallation. This is because no other ablation phenomenon occurs in that region. Based on this difference, the trajectory of the particle can be classified into two types: trajectories penetrating the shock and not penetrating the shock. In order to study the behavior of spalled particles, it is important to evaluate the minimum ejection velocity required to reach the shock. This type of data could also be required to calibrate Particle Tracking Velocimetry measurements or to determine the minimum mechanical energy at the time of ejection.

The chemical interaction of spalled particles with the flow field is also a phenomenon of great interest, especially the computation of the carbon species trail left by the particle. The carbon products released by the spalled particles are expected to radiate energy, but are usually neglected in the radiative heat transfer calculation [95].

4.1 Parametric Study

The path travelled by the particle is a function of its size and ejection parameters (ejection velocity, ejection position, and ejection angle). Hence, a parametric study is conducted to examine the changes in the trajectory of the spalled particle with regards to these parameters. The study is conducted in Mach 5 Argon flow, whose properties have been discussed in Section 3.3. Each parameter is varied by keeping other parameters constant, and its effect on the path of the particle is studied. It should be noted that the particle used for simulation

studies is a pure graphite sphere, as mentioned in the Assumption 1 and Assumption 4 of Section 2.1.

Figure 4.1 shows the effect of the size of the particle on its trajectory while being ejected 3 mm, 7 mm, and 13 mm from the center axis, at a normal initial velocity of 100 m/s. The sizes of the particle considered are 40 μm, 60 μm, and 80 μm, and it is observed that with an increase of size, the particle tend to move further into the flow field, even penetrating the shock.
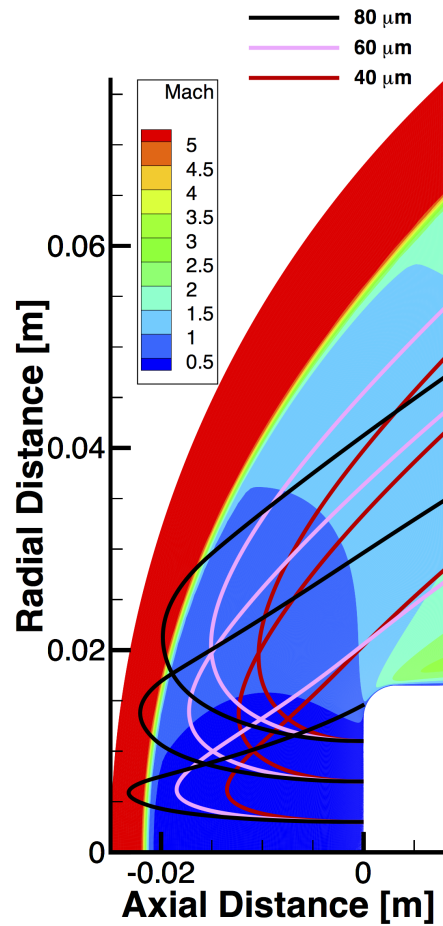
Figure 4.1: Trajectories response to variation of the particles diameter ($V_p = 100$ m/s, $\theta = 0°$)

The effect of ejection velocity on 60 μm particle's path when normally ejected from the surface, 3 mm, 7 mm, and 10 mm from the center axis, is indicated in Figure 4.2. With an increase in the ejection velocity, from 75 m/s, to 100 m/s, to 125 m/s, the particle moves closer to the shock and penetrates it.
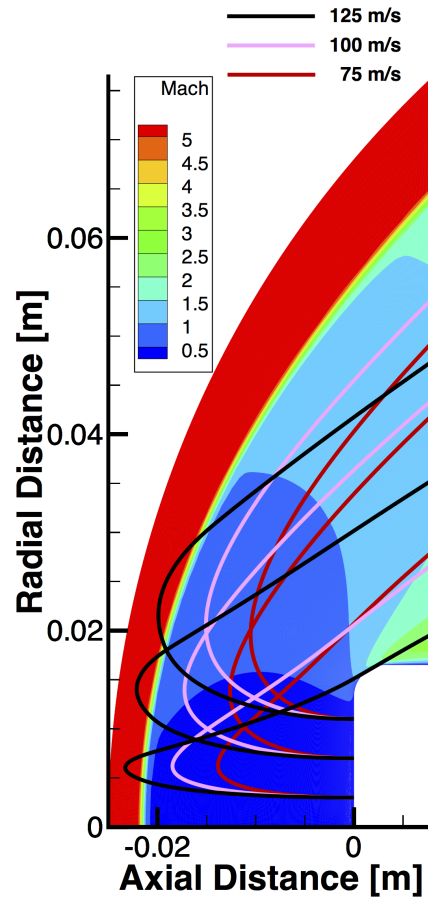
Figure 4.2: Trajectories response to variation of the ejection velocity ($d_p = 60$ μm, $\theta = 0°$)

The trajectory of the particle is also affected by the angle of ejection. Figure 4.3 demonstrates the effect of ejection angle on particle's trajectory of size 80 μm when ejected from the surface, 3 mm, 7 mm, and 11 mm from the center axis, at an ejection velocity of 100 m/s. It is observed that as the angle of ejection approaches to 0°, the particles move further

forward into the flow field. However, it is also noticed that as the angle increases from 0° to 90°, the particles rapidly move away from the centerline.
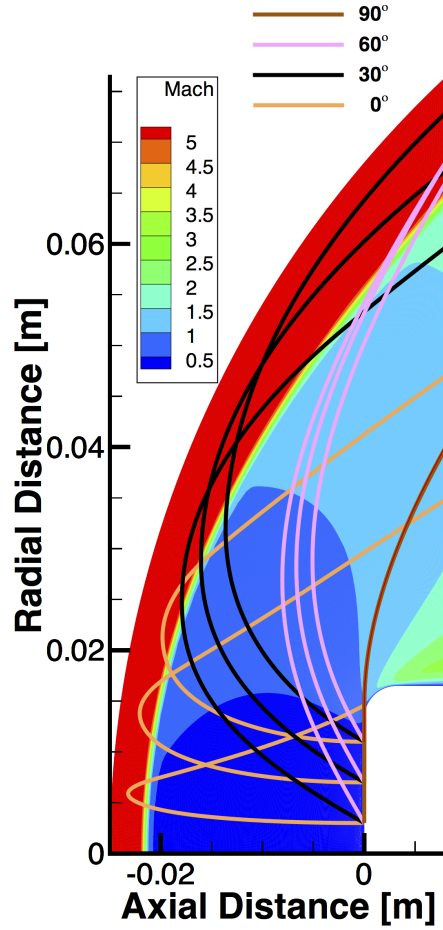
Figure 4.3: Trajectories response to variation of the ejection angle ($d_p = 80$ μm, $V_p = 100$ m/s)

It should be noted that as the ejection position approaches the center axis, the particles traverse more into the flow field and are less directed away from the sample in the downstream region, as can be seen in Fig. 4.1, Fig. 4.2, and Fig. 4.3.

4.2 Simulation in the Argon Flow Field

A test case using argon flow is chosen initially to simplify the problem. The flow field computed for this test case is shown in Figure 3.3. Since argon is a monoatomic gas, the flow field temperature is higher than that of air since the energy cannot be stored in vibrational and rotational modes. Moreover, because argon is a noble gas, the particles are only subjected to sublimation.

Behavior of the particle

As discussed earlier, in an argon flow, the particle is only subjected to sublimation. The sublimation occurs at the particle surface temperature above 3000 K. Due to the low thermal conductivity of argon, the convective heat rates are minimal, and hence, the particle and flow field interaction is limited. This results in little to no recession. Various numerical tests conducted concluded that only particles smaller than 16 μm can reach sublimation temperatures and recess. For instance, a 16 μm particle ejected normally to the surface requires an ejection velocity of 320 m/s to reach the shock, and only a 0.35% change of size takes place due to sublimation. Hence, to evaluate the nature of recessing particle in the argon environment, its size was chosen to be below 16 μm.

To analyze the behavior, Figure 4.4(a) illustrates the path travelled by a particle of 12 μm of initial diameter, normally ejected from the sample surface, at a point 10 mm from the center axis, with a velocity of 380 m/s. The variation of the diameter and temperature of the particle, as well as the energy terms are shown respectively in Figs. 4.4(b) and 4.4(c). The sudden change in the temperature slope occurs when the particle interacts with the shock wave. The re-radiative energy also plays a prominent role among the energy source terms when the particle is ahead of the shock. The interval of time when the particle is ahead of the shock is indicated in the Figs. 4.4(b) and 4.4(c), and also in the subsequent plots. The temperature of the particle and the sublimation heat rate exhibit a sudden rise

in their profile, a few milli-seconds before it exits the computational domain of flow field. At a temperature above 4000 K, the vapor pressure is larger than the atmospheric pressure; and thereby, the vaporizing rate (as given by Eq. 2.21) is in significant order of magnitudes. These conditions result in more mass removal at each time step due to sublimation, which explains the sudden rise in those two profiles.

It is to be noted that the jagged results present in Figure 4.4(c), and in later plots, is not caused by the numerical model, but by the fact that no spatial interpolation is performed when transferring the flow field properties to the trajectory code. The properties in the CFD mesh are assumed to be constant in each cell; therefore, as the particles travel from one cell to an other, the properties change abruptly. Although it is not expected that the results change much, the data would certainly appear smoother if the field properties were spatially filtered.

Minimum ejection velocity

The minimum ejection velocity required by the particle to penetrate the shock relies on the ejection parameters (position, angle, and size). To establish a relation between the minimum ejection velocity and the size of the particle, an ejection normal to the surface is considered to simplify the problem. In addition, the largest value among the minimum ejection velocities, computed at various locations on the sample's surface, is chosen.

The particles smaller than 10 μm need very high ejection velocities (greater than 600 m/s) to pass through the shock. Also, these particles tend to completely vaporize either after entering or re-entering the shock. With low to moderate ejection velocities, these particles travel a path near to the surface of the test piece. The presence of these particles near the surface is considered least effective as their spallation impact is minimal when compared to other ablation mechanisms which provide a greater effect on the sample. For example, the particle of initial size 5 μm travels nearer to the sample surface when ejected normally with
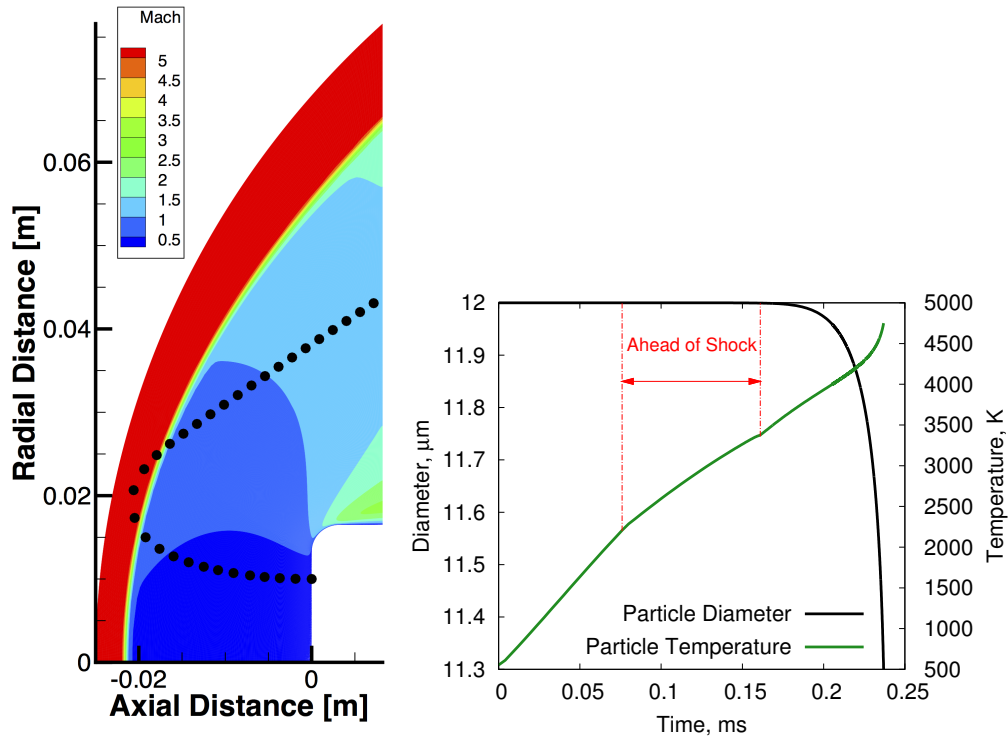
(a) Trajectory of the spalled particle

(b) Variation of diameter and temperature
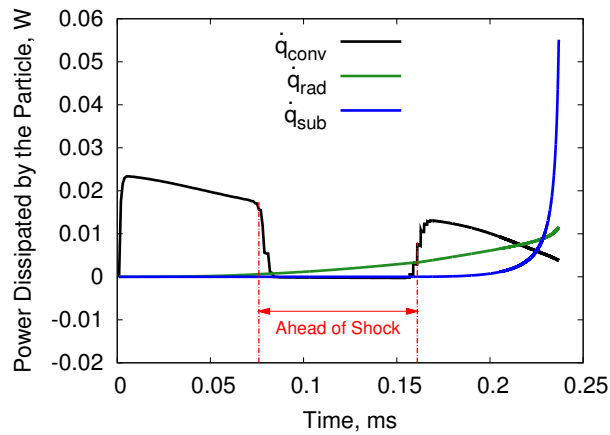
(c) Variation of rates of different heat and energies

Figure 4.4: Trajectory and variations of diameter, temperature and heat energy rate terms of the spalled particle as a function of time in the argon flow field

a velocity of 25 m/s, 7 mm from the center axis, as shown in Figure 4.5. It is also seen that the particle traverses a path relatively closer to the sample surface when ejected with a velocity of 100 m/s. However, when the ejection velocity increases to 400 m/s, the particle tend to vaporize completely in the downstream region of the shock. Similarly, with an initial ejection velocity of 750 m/s, the particle crosses the shock but completely vaporizes before it re-enters.
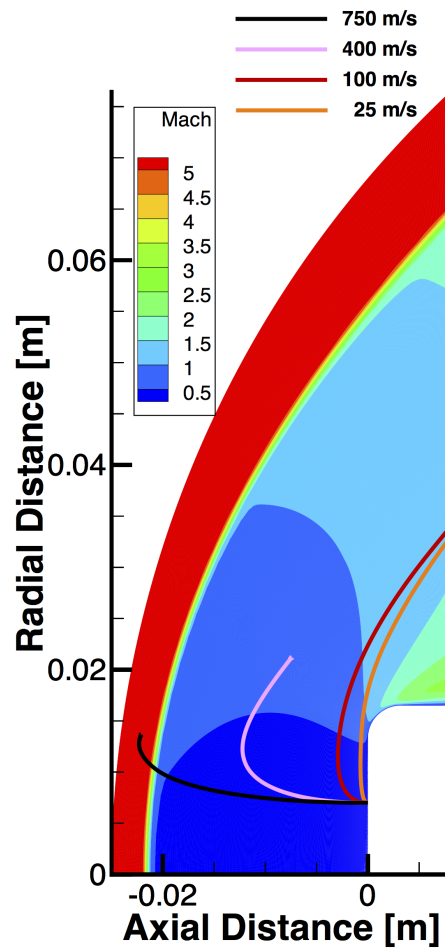
Figure 4.5: Trajectories of 5 μm particle at different ejection velocities in the argon flow field

Figure 4.6 illustrates the variation of minimum ejection velocities needed by the particles to cross the shock as a function of its size. It is observed that with the increase in the particle

size, the minimum ejection velocity decreases.
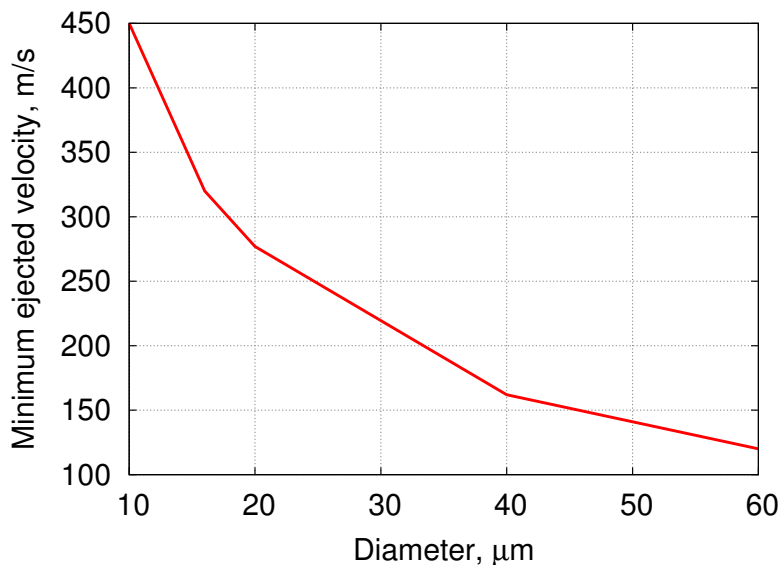
Figure 4.6: Variation of minimum ejected velocity with diameter for the argon flow field

The initial momentum required by the particle to penetrate through the shock is demonstrated in Figure 4.7 with respect to its mass. It is noted that the plot is nearly linear. However, the linearity of the graph is due to the small number of data taken to construct it. It is believed that the graph would appear to have a parabolic shape when continuous data is used.

4.3   Simulation in the Air flow field

The species taken into account for the air flow field, as discussed in Section 3.3, are Ar, N_2, O_2, NO, O, and N. Hence, the particle in this flow field undergoes oxidation and nitridation along with the sublimation process. The behavior of the particle and nature of the surface reactions are analyzed in detail in the following text, and a comparative study of the chemistry model with an other model is performed. As was done in the previous section, the behavior of minimum ejection velocities with respect to size is presented.
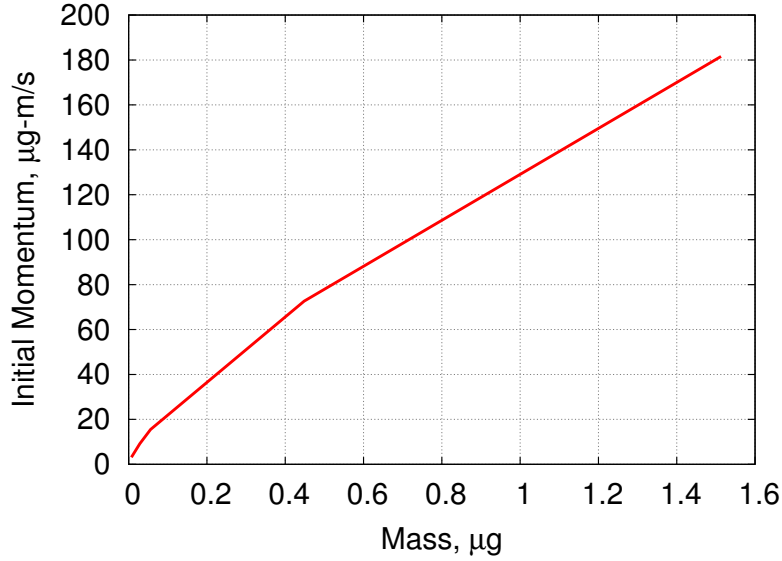
Figure 4.7: Variation of initial momentum of the particle with its mass for the argon flow field

Behavior of the particle

The recession in the diameter of the particle is due to its chemical interactions with the flow field (oxidation, nitridation and sublimation). The oxidation and nitridation of the particle depend on the concentration of species responsible for the reaction, whereas the sublimation of the particle is a function of its surface temperature. Figure 4.8(a) shows the trajectory of the spalled particle of initial size 15 μm ejected normally with a velocity of 135 m/s, 4 mm from the axis of the sample. Figs. 4.8(b) and 4.8(c) illustrate the variation of the diameter and surface temperature of the particle, and the energy terms. The particle recesses immediately after ejection. This is in contrast to the behavior in the argon flow field where the particle recesses only after reaching the sublimation temperature. The discontinuities in the diameter and temperature profiles in Fig. 4.8(b) occurs when the particle interacts with the shock. It is also observed that the convective and reaction heat rates of the particle ahead of the shock are nearly zero and only the re-radiative energy is the effective one, as shown in Fig. 4.8(c).
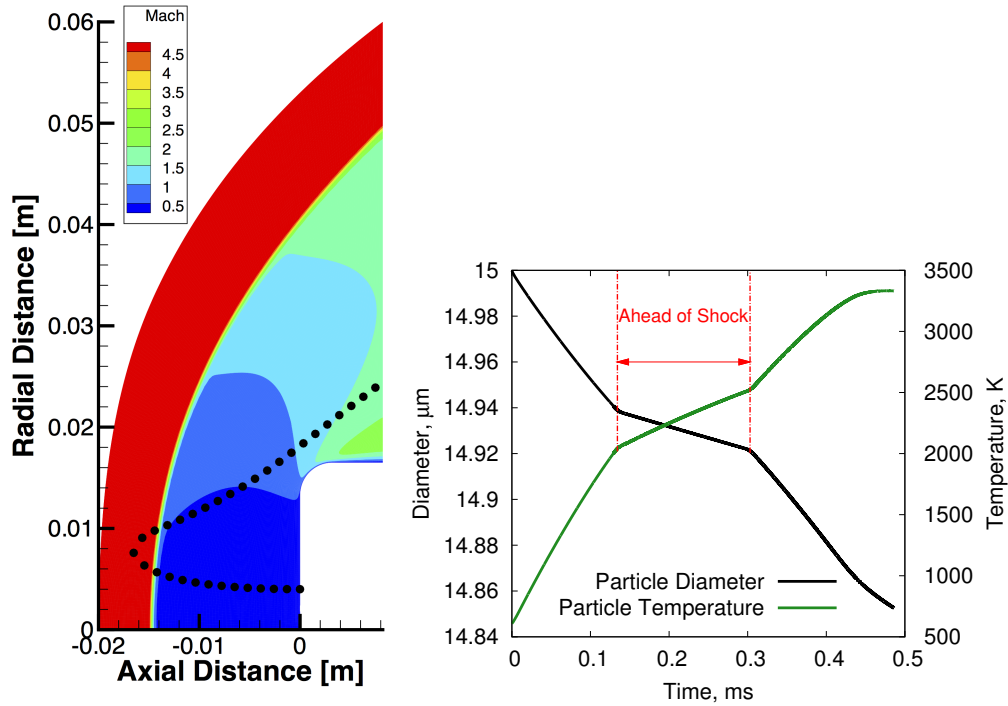
48

(a) Trajectory of the spalled particle

(b) Variation of diameter and temperature
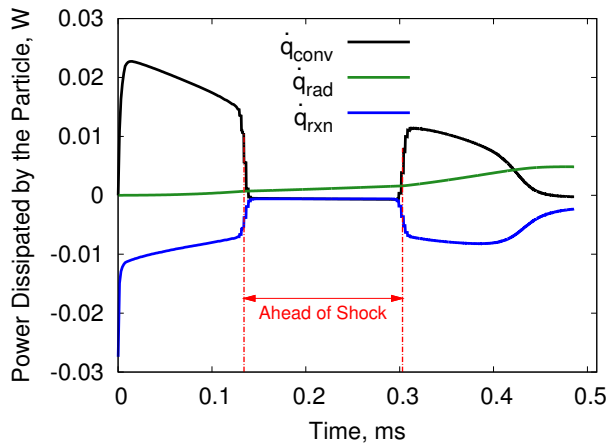
(c) Variation of rates of different heat and energies

Figure 4.8: Trajectory and variations of diameter, temperature and heat energy rate terms of the spalled particle as a function of time in the air flow field

Chemical-behavior of the particle

It is observed, from various numerical tests, that the oxidation rates are higher than nitridation and sublimation for the spalled particle. The production rates are very low for the nitridation reaction owing to a very low reaction efficiency γ_0. However, the oxidation and nitridation production rates are high near the surface of the sample due to high species concentration at the wall. The particle barely sublimates in this flow field as it does not reach the sublimation temperature.

The effect of size of the particle on its surface reactions is studied. Figure 4.9(a) shows the path traversed by 25 μm and 35 μm particles ejected normally at a velocity of 75 m/s, 8 mm from the center axis. It is noticed that the 35 μm particle penetrates through the shock, whereas the 25 μm particle does not, as shown in Fig. 4.9(a). The variation of production rates due to oxidation, nitridation, and sublimation as a function of size of the particle are illustrated in Figures 4.9(b), 4.9(c), and 4.9(d). It can be seen that an abrupt change in the oxidation and nitridation production rates when the particle crosses the shock. The production rates are constant in the free stream region due to approximately zero concentrations of O and N and very little concentration of O_2. As expected, the production rates due to sublimation are higher for the particle that does not penetrate the shock.

Also, the effect of ejection velocity on the particle's surface reactions is studied. The trajectories of the 20 μm particle ejected normally from the surface, at a point 6 mm from the center axis, with velocities of 80 m/s and 125 m/s are shown in Figure 4.10(a). The particle ejected at 80 m/s does not penetrate the shock, whereas the particle ejected at 125 m/s penetrate. Figures 4.10(b), 4.10(c), and 4.10(d) illustrate the variation of production rates with the ejection velocities of the particle. The production rates show similar behavior as a previous test-case for their respective trajectories.

However, the chemical behavior of the particles show a high production of CO, which is in contrast to spectroscopic measurements indicating the presence of CN ahead of the shock.

(a) Trajectory

(b) Oxidation

(c) Nitridation

(d) Sublimation
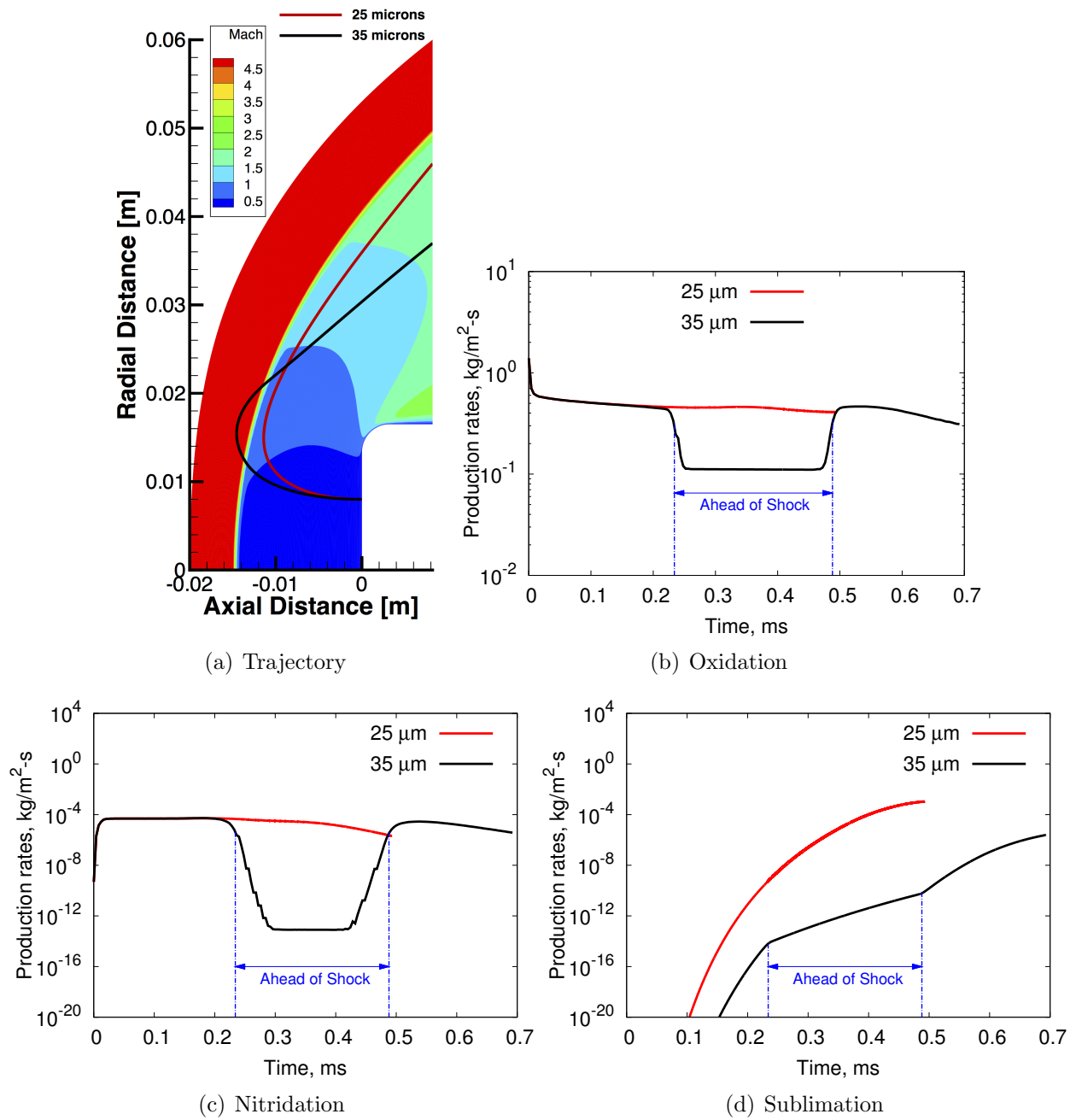
Figure 4.9: Flow interactions for spalled particles of various size, ejected normal to the surface at 75 m/s, 8 mm from the center line

51

(a) Trajectory

(b) Oxidation

(c) Nitridation

(d) Sublimation
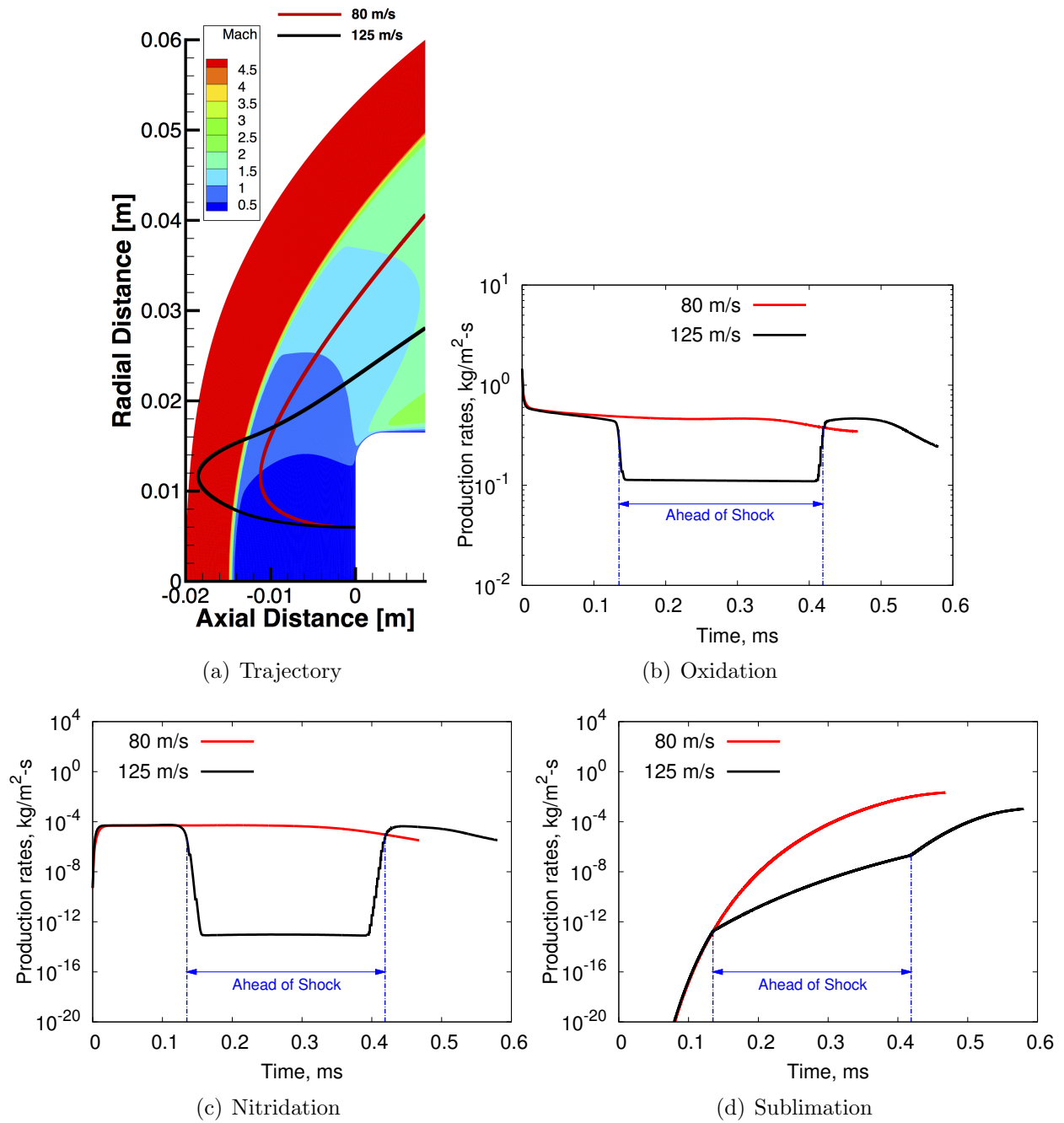
Figure 4.10: Flow interactions for 20 μm spalled particle of various initial velocities, ejected normal to the surface at 6 mm from the center line

The possible traces of CN can be a result of carbon vapor (C_1, C_2, C_3) reacting with nitrogen (both atomic and molecular). Since the sublimation production is minimal, the reaction is likely to yield a minuscule production. Hence, the presence of CN is most likely due to CO undergoing following gas phase reactions:

$$CO + N \rightleftharpoons CN + O$$

$$CO + N_2 \rightleftharpoons CN + NO$$
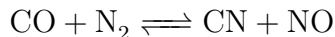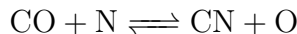
Comparison with Park's model

The chemistry model of the code, used to account for the chemical interactions of the spalled particle, is compared with Park's model [69, 70, 96]. The values of γ_0 and E_R for Park's chemistry model are given in Table 4.1. Park's model considers the sublimation model, and only vaporization to C_3 as it is the dominant product. Hence, the comparison in sublimation is only made for C_3 production rates.

Table 4.1: Values of γ_0 and E_R for the following reactions according to Park's surface chemistry model

Reaction	γ_0	E_R (kJ/mol)
$C(s) + O \longrightarrow CO$	0.63	9.644
$2\,C(s) + O_2 \longrightarrow 2\,CO$	0.50	0
$C(s) + N \longrightarrow CN$	0.30	0
$3\,C(s) \longrightarrow C_3$	5.19×10^{13} (γ_{sub})	775.81

For the comparison, a 30 μm particle is ejected at a normal ejection velocity of 90 m/s from the surface, 10 mm from the center axis. Figure 4.11 illustrates the comparative results. Although the particle follows the same trajectory, it is noticed that the variation of diameter and temperature along its path are different, as can be seen in Figure 4.11(a). Park's model vaporizes comparatively less than the model used in this work.

The oxidation rates of Park's model, as shown in Figure 4.11(b), do not differ much with the present model except at the surface of the sample. However, the sublimation rates are roughly 1000 times lower for Park's model when compared with the model used in this work, as shown in Figure 4.11(d). It should be noted that the sublimation behavior, which is the function of the surface temperature of the particle, is same for the two models. The different surface temperature profiles of two models, as can be seen in Figure 4.11(a), attribute to the huge difference between their sublimation rates. Similarly, the nitridation rates are approximately 100 times higher for Park's model, as seen in Figure 4.11(c). The dramatic difference between the rates is due to the value of γ_0 for nitridation in Park's model, which is significantly higher. Since, the production rates of sublimation reactions are comparatively lower, the particle more likely undergoes oxidation and nitridation reactions.

The reaction efficiency γ_0 for nitridation is relatively higher for Park's model and hence, ensures high production rates. However, in mid 60's, Goldstein [97] performed experimentation, on TSX and AGOT graphite samples, by resistively heating them and exposing to a microwave-discharged nitrogen to quantitatively investigate the reaction efficiency of nitridation. It was found from the experiments that the efficiencies were ranged from 0.41×10^{-3} to 1.7×10^{-3} for TSX graphite, and 0.45×10^{-3} to 0.69×10^{-3} for AGOT graphite, which concludes that one in every 1000 atoms of nitrogen impinging on graphite react. Later, Suzuki et. al. [98, 99] performed tests on isotropic graphite to study the ablation in pure nitrogen flows using an inductively coupled plasma wind tunnel. It was observed from the results that the reaction efficiency was in the range of 2.5×10^{-3} and 3.2×10^{-3} for temperatures about $1822 - 2184$ K, and was in the range of 1.4×10^{-3} at 1400 K. Furthermore, Suzuki et. al. [100, 101] developed a numerical model and noticed that with a reaction efficiency set to 3.2×10^{-3}, the experimental and numerical data were in good agreements. And recently, Zhang et. al. [102] performed experimentation on high-purity graphite exposed to a N/N_2 mixture in a furnace-heated quartz flow tube coupled to a microwave discharge system. The

(a) Diameter and Temperature

(b) Oxidation

(c) Nitridation
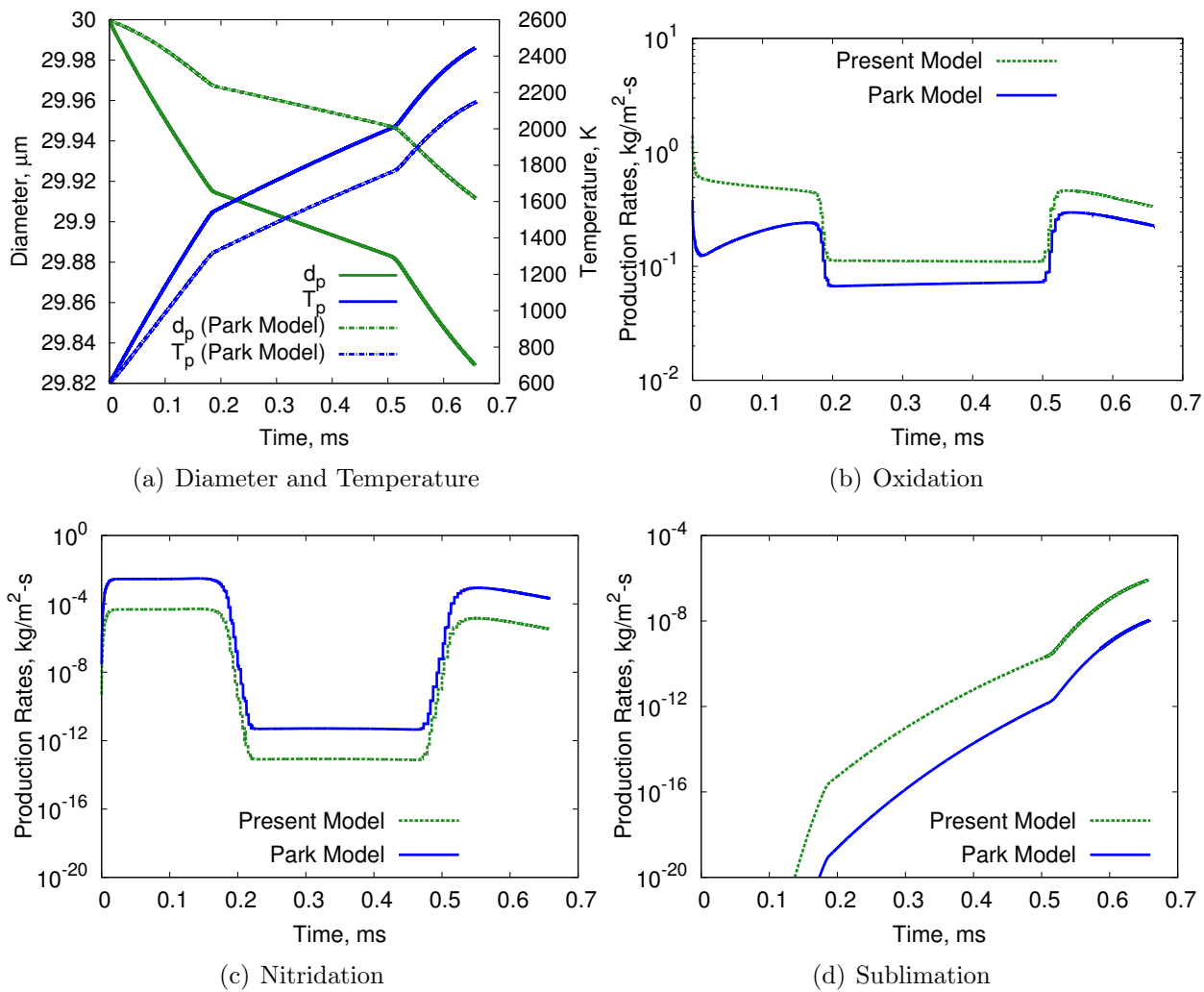
(d) Sublimation

Figure 4.11: Comparison of variation of diameter and temperature of particle and production rates of oxidation, nitridation and sublimation with Park's Model

results demonstrated an average value of 3×10^{-3} for nitridation reaction efficiency at 1273 K. The above experimental studies indicate that the γ_0 for carbon nitridation reaction is at least two order of magnitudes less than the one listed in Park's model. This supports the production rates of nitridation reaction computed by the code. The chemistry model used in the code is probably more accurate as the order of magnitude of the reaction efficiency is similar to the one predicted by the experimental studies.

Minimum ejection velocity

The distance of the shock from the test piece is comparatively less in the air flow field than in the argon flow field. Hence, minimum ejection velocity needed to penetrate the shock is relatively less than in the argon flow field. As an example, a 10 μm sized particle requires a minimum velocity of 150 m/s in the air flow field compared to 450 m/s in the argon flow field to penetrate through the shock. Figure 4.12 demonstrates the variation of minimum ejection velocities required to cross the shock as a function of the diameter of the particle.
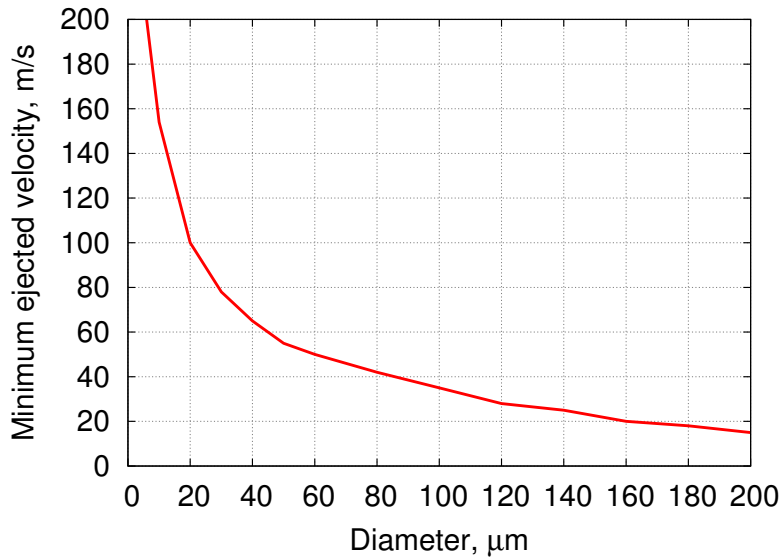
Figure 4.12: Variation of minimum ejection velocity with diameter for the air flow field

Figure 4.13 illustrates the variation of initial momentum required by the particles to

penetrate throughout the shock with respect to its mass. It is noticed that the graph is parabolic in shape. However, a more continuous data would give a smoother curve.
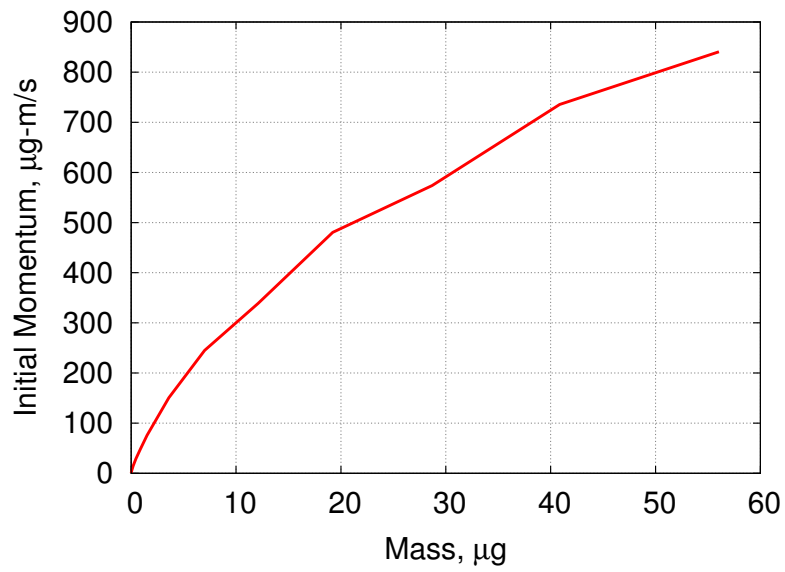
Figure 4.13: Variation of initial momentum of the particle with its mass for the air flow field

Chapter 5 Results – Two-way Coupling

The developed spallation code uses the CFD solution, through one-way coupling, to simulate the spalled particle trajectories. The simulations take into account the effect of flow field properties on the particles. To evaluate the spallation phenomenon, it is also important to take into consideration the effect of particles on the flow field. To achieve this, a loose-coupling between the spallation code and KATS CFD code is performed, and only mass coupling is considered in this work.

5.1 KATS CFD

KATS is a laminar Navier-Stokes solver that computes thermo-chemical non-equilibrium flow fields in continuum regime [103]. The governing equations of the solver are of form:

$$\frac{\partial \mathbf{Q}}{\partial t} + \nabla.\left(\mathbf{F} - \mathbf{F_d}\right) = \mathbf{S} \tag{5.1}$$

where $\mathbf{Q}$ is the vector of conservative variables, $\mathbf{F}$ and $\mathbf{F_d}$ are convective and diffusive fluxes respectively, and $\mathbf{S}$ is the source vector. The elements of the conservative variables vector and source vector are represented as:

$$
\mathbf{Q} = \begin{pmatrix} \rho_1 \\ \vdots \\ \rho_{ngs} \\ \rho_g u \\ \rho_g v \\ \rho_g w \\ E \end{pmatrix} \qquad \mathbf{S} = \begin{pmatrix} \dot{\omega}_1 \\ \vdots \\ \dot{\omega}_{ngs} \\ 0 \\ 0 \\ 0 \\ 0 \end{pmatrix} \tag{5.2}
$$

where ρ_i is the density of species i, (u, v, w) are bulk velocity components, E is the total energy, $\dot{\omega}_i$ is the mass production rate introduced by species i, subscripts from 1 to ngs represent the number of species, and subscript g represent the gas mixture.

5.2 Mass coupling

The surface reactions on the particle yield gaseous products, which are deposited in the flow. In order to analyze the particle effects on flow field, the source terms from Eqs. 2.18, 2.19, and 2.21 are added to the governing equation of KATS (Eq. 5.1) and is given by:

$$
\dot{\omega}_i = \frac{\dot{m}_{\mathrm{C}/i}}{V} \tag{5.3}
$$

where i is CO, CN, sub (C_1, C_2, C_3), and V is the volume of the mesh cell in which the spalled particle is present [104].

5.3 Cell center locating code

The source vector matrix $\mathbf{S}$ is computed at the cell centers of the mesh. Since the developed spallation code uses extrapolated nodal values of flow field properties, a new algorithm is developed to locate the center of the mesh cell in which the particle is present. Figure 5.1

59

illustrates the trajectory of a 30 μm particle ejected normally from the surface, 5 mm from the center axis, at an initial velocity of 90 m/s in the air flow field. The figure also shows the cell centers computed by the code (denoted by red squares) at three different locations with respect to the position of the particle.

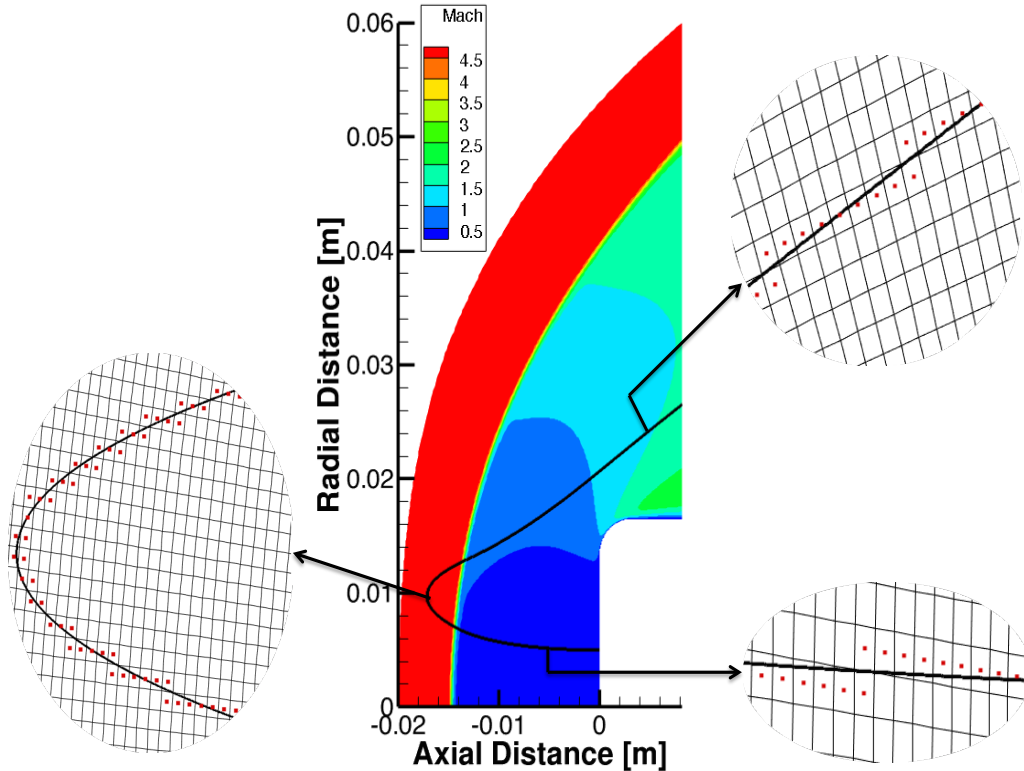Figure 5.1: Computed cell-centers with regards to the trajectory of the particle

5.4 Loose-coupling solution procedure

Initially, the particle surface reaction products $(CO, CN, C_1 + C_2 + C_3)$ are included in matrix $\mathbf{Q}$ as new elements. The density of the new species is assumed to be zero and is computed until a converged solution is obtained. Simultaneously, the spallation code is made to cal-

culate the source terms based on Eq. 5.3 and corresponding cell centers along the path of the particle. The steady state flow field solution is made transient by adding the spalled particles source term in the matrix $\mathbf{S}$ at the respective cell center. In order to produce a time accurate transient solution, Courant-Friedrichs-Lewy (CFL) number is restricted under 1. Therefore, the source term file is modified, by linearly interpolating the production rates between the time steps, therefore making the spallation code and CFD code time step sizes equivalent.

5.5 Verification procedure

To verify the loose-coupling procedure, a constant spallation source term is added to a zero velocity flow field. An integration is performed over the cell volumes of the mesh to evaluate the mass deposited by the spalled particle in the flow field. It was observed that the mass evaluated through integration method was equal to the total mass added from the source term file (constant source term value $\times$ time step size $\times$ total time steps). Therefore, the loose coupling method considered is free from errors.

5.6 Time-accurate loose-coupling solutions

For the loose coupling, simulations in the argon flow field environment are considered. The effect of a 14 μm particle, which is ejected normally at a velocity of 370 m/s and 13 mm from the center axis, on the argon flow field is illustrated in Figs. 5.2, 5.3, 5.4, and 5.5. To achieve a time accurate solution, the time step size of 4×10^{-9} (which corresponds to a maximum CFL of 0.824) is chosen for the CFD code. The spalled particle takes 0.2697 milliseconds of time to travel through the computational domain of the flow field. Since the particle is subjected to only sublimation in argon flow, the effect of carbon vapor $(C_1 + C_2 + C_3)$ on the flow field is demonstrated in the figures below at different trajectory points. The figures consist of temperature and carbon vapor density profiles of the argon flow field at

different travel times of the particle. The temperature profile is used to assess the position of the particle with respect to shock and the temperature zone through which it is passing through. The carbon density profile determines the effect of mass source term deposited by the particle in the flow field.

Figure 5.2 illustrates the simulations at 70 microseconds of particle travel. As the particle approaches the shock, its surface temperature is less than the sublimation temperature, so no recession takes place. It should be noted that the temperature of the particle and flow field are not the same, and due to the low thermal conductivity of argon, the interaction of the particle with the fluid is limited.

On Figure 5.3, the particle is now ahead of the shock. At 0.147 millisecond of particle travel, the particle sublimates and starts releasing carbon vapor. The transport property (diffusivity in this case) is a function of surface temperature of the particle. The released vapor is diffused in the fluid flow, and its mobility is proportional to the magnitude of diffusivity. Additionally, the bulk velocity of the flow field directs the diffused vapor along the downstream region of the shock. The above-described behavior of the carbon vapor can be observed in Figs. 5.3, 5.4, and 5.5.

With an elevation of the surface temperature of the particle, the concentration of carbon vapor increases as shown in Figure 5.4. At a travel time of 0.2 milliseconds, the particle is still in the upstream region of the shock and is about to re-enter it. It can also be seen that the fluxes tend to diffuse in lateral directions with an increased mobility.

As the particle re-enters the shock and more into the downstream region, the concentration of the carbon vapor increases in magnitudes and get diffused around the particle. Figure 5.5 shows the simulation at particle's travel time of 0.26 milliseconds.

It is important to note that the presence of carbon vapor in the upstream region of the shock coincides with the spectroscopic observations [40, 41]. This reinforces the hypothesis that the presence of spalled particles ahead of the shock are the reason for the spectroscopic

62
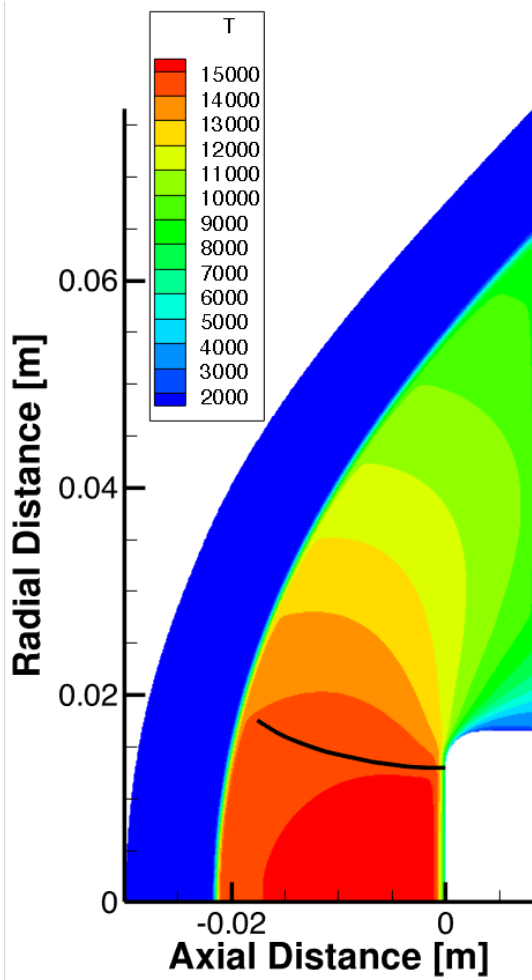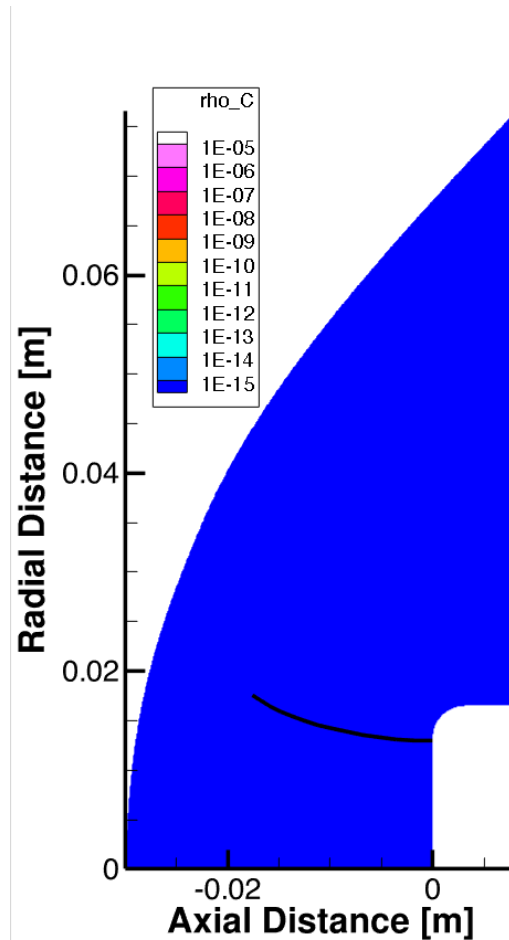
(a) Temperature (b) Carbon Density

Figure 5.2: Trajectory of the particle in temperature and carbon density profiles of the argon flow field at 0.07 milli seconds
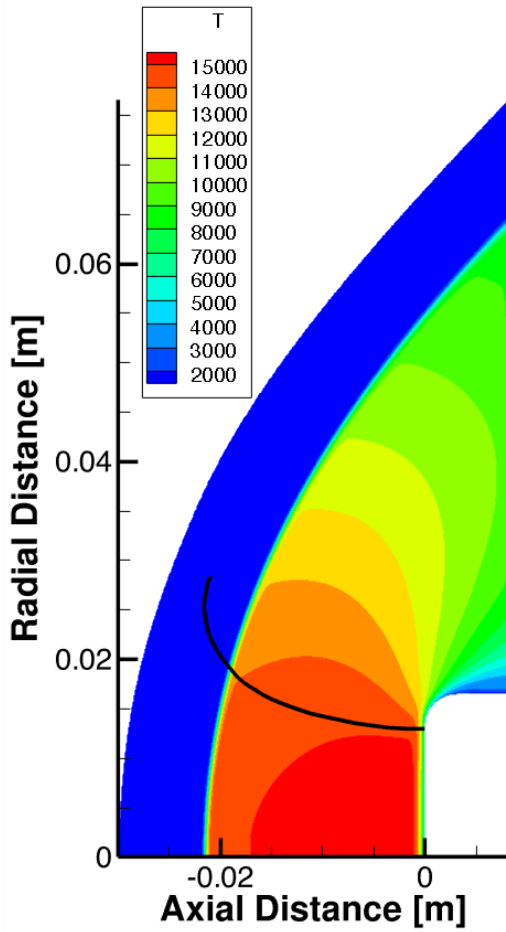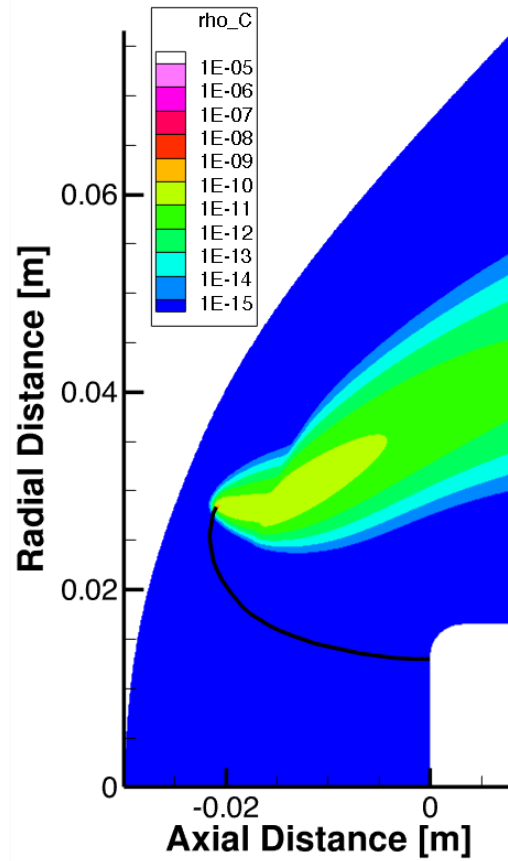
(a) Temperature (b) Carbon Density

Figure 5.3: Trajectory of the particle in temperature and carbon density profiles of the argon flow field at 0.147 milli seconds
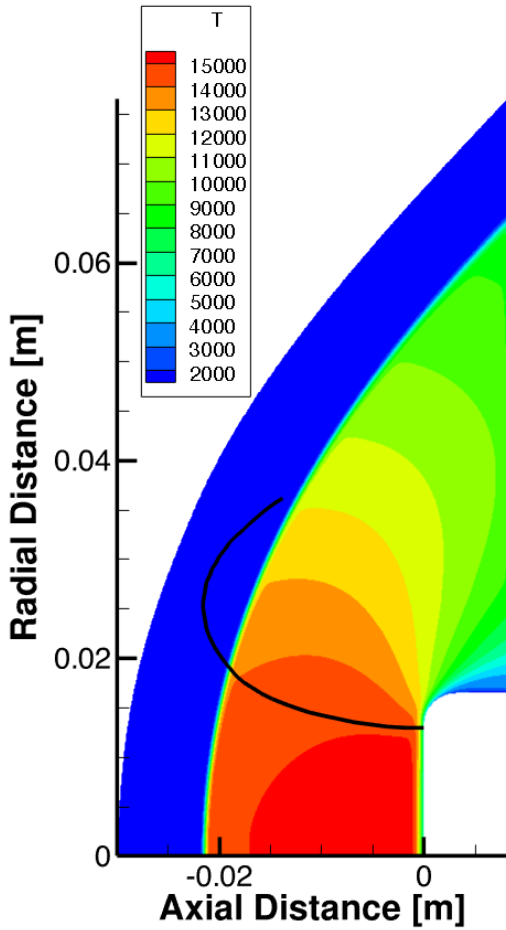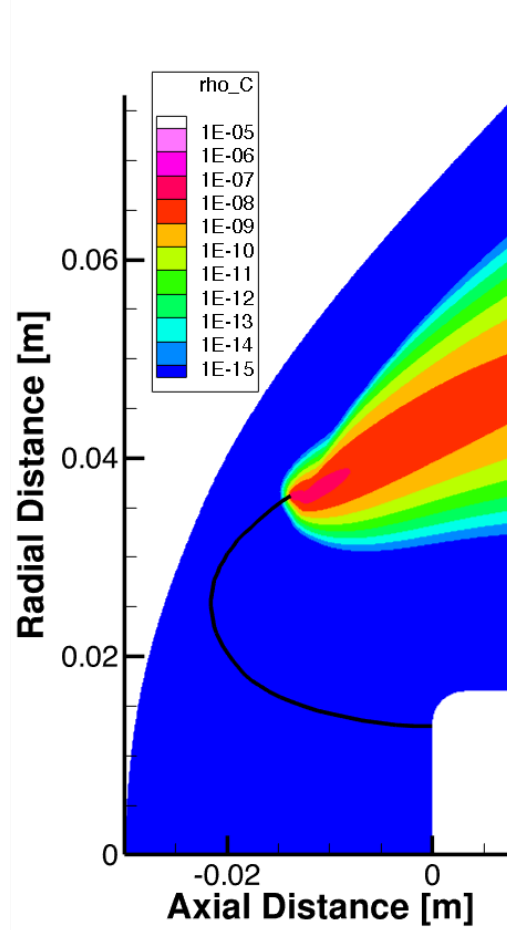
(a) Temperature   (b) Carbon Density

Figure 5.4: Trajectory of the particle in temperature and carbon density profiles of the argon flow field at 0.2 milli seconds
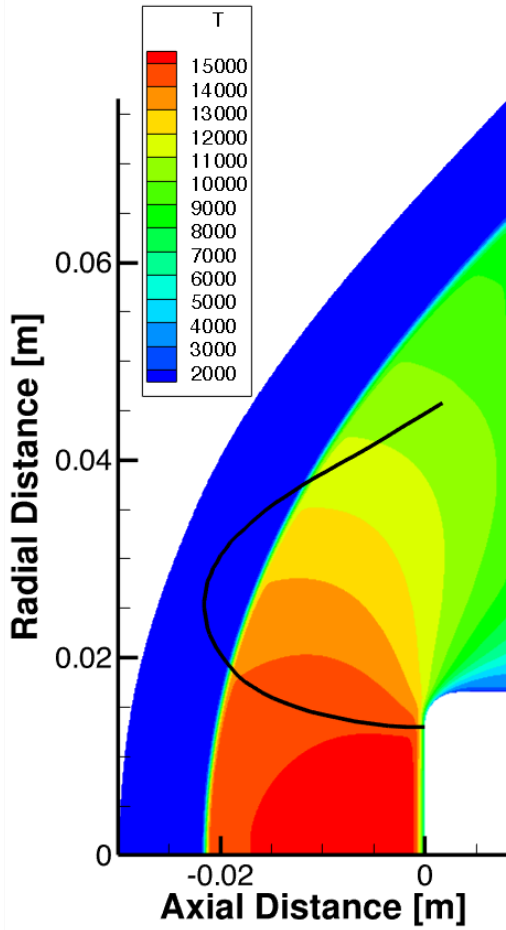
(a) Temperature
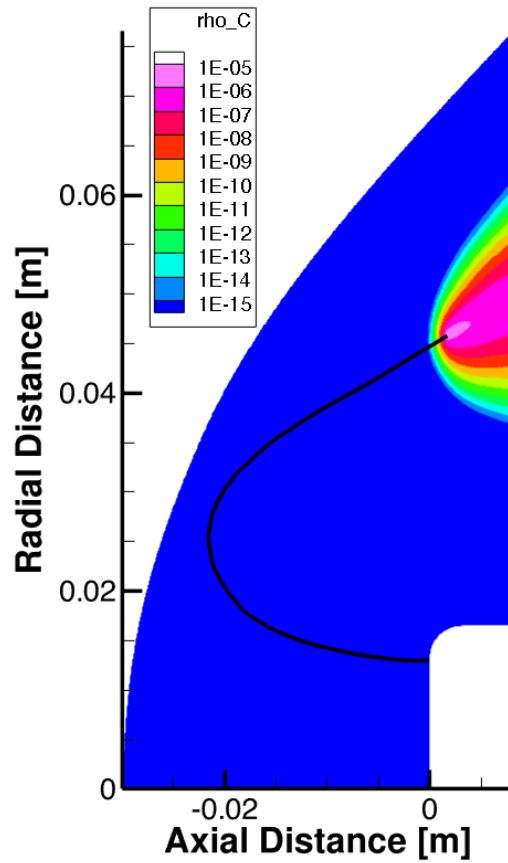
(b) Carbon Density

Figure 5.5: Trajectory of the particle in temperature and carbon density profiles of the argon flow field at 0.26 milli seconds

emissions in that region. It should be also noted that the concentration of the carbon vapor produced by a single particle is in moderate orders of magnitude and is ought to be effective in modifying the aerodynamic heat rates at the surface of the sample.

Chapter 6 Summary and Conclusions

6.1 Summary

A code was developed which accounts for the dynamics and chemical behavior of the spalled particle. In order to analyze the spallation phenomenon, the code was one-way coupled to the solution field obtained from a hypersonic aerothermodynamic CFD code. The developed code solves the mass, momentum, and energy conservation equations to compute the spalled particle properties. The chemistry model of the developed code accounts for oxidation, nitridation, and sublimation reactions at the surface of the particle. The parameters required for evaluating the rate constants for surface reactions are chosen from Driver's model.

In order to ensure that the developed code is free from implementation errors and solves the equations correctly, the Method of Manufactured solutions is applied to verify the developed code. The verification results concluded that the system of equations retain the order of accuracy, and the developed code is deemed free from mathematical errors.

The flow field solutions of a Mach 5 high enthalpy Argon and Air flow over a sample are used to one-way couple the spallation code and study the spalled particle behavior. The boundary conditions to generate the solution were also discussed.

Next, parametric tests were conducted to study the variation of trajectories traversed by the spalled particles as a function of its size and ejection parameters.

Simulations were computed for a hypersonic flow over a sample, in arc-jet conditions, using argon and air flow fields. The properties of the particle and its energy variations were studied on in detail. Also, the chemical behavior of the particles was studied behind and in front of the shock. A numerical study on variation of production rates of surface reaction products (CO, CN) and carbon vapors (C, C_2, and C_3) as a function of the size of the

particle and ejection velocity was performed. It was observed that the production rates of oxidation reaction were higher when compared to the nitridation and sublimation. Later, the chemistry model used in the developed code was compared with Park's chemistry model. It was noticed that though oxidation production rates are roughly similar, the production rates of nitridation reaction are higher and that of sublimation reactions are lower in the Park's model when compared with the model used in this work.

Furthermore, the minimum ejection velocity required to pass through the shock was computed as a function of a particle's size for both of the flow field solutions. The computed values were found to be relatively very high for the argon flow, when compared with that for the air flow.

Finally, the developed code was loosely coupled to the KATS CFD code and was tested for the argon flow field. A spallation test case was considered and time accurate solution was computed and studied.

6.2   Conclusions

Based on the conducted study, the following list of conclusions are made:

1. **Variation of paths traversed as a function of size and ejection parameters**
   The parametric study conducted depicts that with an increase in the mass or ejection velocity, the particle tends to move further into the flow field and pass through the shock. In contrast, the particle is inclined to penetrate through the shock with a decrease in the ejection angle from $\pi/2$ to 0 radians. Furthermore, the farther the ejection position from the centerline, the more pushed away are the particles from the sample.

2. **Limited sublimation in the argon flow**
   It is observed that in the argon flow field, the particles of size greater than 16 μm hardly vaporize. However, particles smaller than 10 μm need a very high velocity to

69

cross the shock, whereas those with the moderate velocities travel close to the sample. Hence, the possible carbon vapor produced in the upstream region of the shock may be contributed by the particles of sizes between 10 µm and 16 µm. Also, the particles in this range undergo minimal sublimation and hence, deposit a very low amount of carbon traces in the flow field.[1]

3. **Presence of CN as found by spectroscopic measurements**

The spectroscopic measurements conducted in the past indicated the presence of CN emission spectra in the flow, particularly ahead of the shock. However, the production rates from the simulations in the air flow indicate a very low yield of CN and conversely, a high yield of CO from the respective reactions. Therefore, it is suggested that the possible traces of CN are likely produced by following exchange reactions:

$$CO + N \rightleftharpoons CN + O$$

$$CO + N_2 \rightleftharpoons CN + NO$$
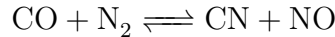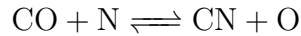
The sublimation vapor produced by the particle is minimal and hence, the production of CN species from the reactions taking place between carbon vapor and nitrogen (both atomic and molecular) is also very low. The production of CN is most likely due to the oxidation product (CO) undergoing further gas phase reactions.

4. **A more accurate chemistry model**

On comparing the chemistry models, though oxidation production rates were approximately similar, there was a drastic difference between the nitridation and sublimation rates. As mentioned above, the chemistry model used in the code yields CN through oxidation reactions. In contrast, the production of CN is originated directly from the nitridation reaction in Park's model. Hence, it is required to evaluate a more accurate

---

[1]This conclusion is based on study conducted on Mach 5 high enthalpy argon flow and should not be considered as general behavior in argon flow.

model among the two models compared. Various experimental studies conducted in the past determined the reaction efficiency for nitridation reaction to being two order of magnitudes less than the one in park's model. Hence, a more accurate chemistry model would be the one used in the code as it shares the same order of magnitude with the experimental results.

5. **Comparison of minimum ejection velocities**

It was also noticed that the minimum ejection velocities necessary to penetrate the shock are significantly higher for the argon flow, about one-third of those values for the air flow. This is due to a larger distance between the shock and the sample for the argon flow when compared with the air flow. This distance is a function of fluid properties and plays a prominent role in assessing the minimum ejection velocities for the flow.

6. **Moderate diffusive flux in the argon flow field**

The time accurate transient solution of the spallation code loosely coupled with the CFD code is presented. The solution in the argon environment concluded that the concentration of sublimation vapor deposited by a single particle was low in the upstream and moderate in the downstream region of the shock. The order of magnitude of the carbon density suggested that the vapor might be effective in altering the aerodynamic heat rates at the surface of the sample. Also, diffusive flux computed through loose coupling provides a possible relationship between presence of spalled particles and the spectroscopic emissions, observed ahead of the shock.

6.3   Original contributions

The following are the original contributions to the field of spallation phenomenon in ablative heat shields:

71

1. **A particle tracking code which computes the dynamics and chemistry of the spalled particles**

   Although various numerical models were developed to compute spalled particle dynamics [66, 69, 71, 74], some models assumed a constant mass and others assumed only sublimation as the chemistry behavior possible for the particle. In this work, the code integrates the models developed by Davies et. al. [66], Pace et. al. [71], and Nozawa et. al. [74], and builds on them by including oxidation and nitridation reactions of spalled particles. The code also tracks the carbon trails as particles travel through the flow field.

2. **Parametric study to understand the effect of size and ejection parameters of the particle on its trajectory**

   The path travelled by the particle is a function of its size and ejection parameters. A parametric study was conducted to study the behavior of the trajectory with respect to these parameters.

3. **A brief study on the behavior of spalled particles in the argon and air flow field**

   To analyze the nature of the spalled particle, the developed code uses the CFD solution, through one-way coupling, to simulate the high enthalpy gas flow field of an arc-jet environment over an light-weight ablative test piece [79, 103]. The flow field solutions of the Mach 5 Argon flow, and Air flow are chosen and a study is performed to understand the behavior of spalled particles in these environments.

4. **Comparison of the proposed chemistry model with the one from the literature, to understand the chemical behavior of the particles**

   As said above, various numerical models constructed to study the spalled particle behavior considered only the sublimation behavior. A chemistry model was included to

account for the oxidation, nitridation, and sublimation nature of the particles, and chemical behavior was examined. The carbon products released by the spalled particles, CN especially, are expected to radiate energy. The code also used an another chemistry model [69, 70, 96], and a comparative study was performed to evaluate the chemical interactions of the particle. Taking spectroscopic results [40, 41] into considerations and based on experimental studies [97, 98, 99, 100, 101, 102], a more accurate model was chosen. Moreover, a likely reason for the presence of CN, as detected by spectroscopic measurements ahead of the shock, was explained.

5. **Evaluation of minimum ejection velocity required by the particle to penetrate the shock in the argon and air flow fields**

The minimum ejection velocities required by the particle to penetrate the shock as a function of its size are calculated for the argon and air flow fields. This type of data could be needed to calibrate Particle Tracking Velocimetry measurements and to determine the minimum mechanical energy at the time of ejection.

6. **Loose coupling between spallation code and KATS CFD code**

Two-way coupling in a lagrangian frame of reference between spallation module and flow field module was not attempted in the past. In this work, a loose coupling between spallation and KATS CFD code is performed. This helps in evaluating the effect of spalled particles on flow field thereby, determining the importance of spallation phenomenon.

Bibliography

[1] "Returning from Space: Re-entry," Section 4.1.7, Federal Aviation Administration, pp. 309–339.

[2] SpaceX, *"SpaceX completes CRS-4 mission for NASA"*, November 2014, Retrieved from: `http://www.spacex.com/news/2014/11/04/spacex-completes-crs-4-mission-nasa`.

[3] Chapline, G., Rodriguez, A., Snapp, C., Pessin, M., Bauer, P., Steinetz, B., and Stevenson, C., "Thermal Protection Systems," *Engineering Innovations*, NASA.

[4] Sherman, M. M., "Entry Thermal Protection," *NASA Space Vehicle Design Criteria (Structures)*, SP-8014, NASA, August 1968.

[5] Neuse, E. W., "Polymers for potential use as charring ablators under hyperthermal re-entry conditions: A review of recent developments," *Materials Science and Engineering*, Vol. 11, No. 3, 1973, pp. 121–150.

[6] Venkatapathy, E., Laub, B., Hartman, G., Arnold, J., Wright, M., and Allen, G., "Selection and certification of TPS: constraints and considerations for Venus missions," *6th Interplanetary Probe Workshop*, Atlanta, GA, June 21-22 2008.

[7] Laub, B., Wright, M. J., and Venkatapathy, E., "Thermal Protection System (TPS) Design and the Relationship to Atmospheric Entry Environments," *6th International Planetary Probe Workshop*, Atlanta, GA, June 21-22 2008.

[8] Suzuki, K., Kubota, H., Fujita, K., and Abe, T., "Chemical Nonequilibrium Stagnation Ablation Analysis of MUSES-C Superorbital Re-Entry Capsule," *Journal of Spacecraft and Rockets*, Vol. 35, No. 3, 1998, pp. 407–409.

[9]   Ishii, N., Yamada, T., Hiraki, K., and Inatani, Y., "Reentry Motion and Aerodynamics of the MUSES-C Sample Return Capsule," *Transactions of the Japan Society for Aeronautical and Space Sciences*, Vol. 51, No. 172, 2008, pp. 65–70.

[10]   Olynick, D., Chen, Y. K., Tauber, M., and Chen, Y. K., "Forebody TPS sizing with radiation and ablation for the Stardust Sample Return Capsule," *32nd Thermophysics Conference*, AIAA Paper 1997-2474, 1997.

[11]   Olynick, D., Chen, Y. K., Tauber, M., and Chen, Y. K., "Wake flow calculations with ablation for the Stardust Sample Return Capsule," *32nd Thermophysics Conference*, AIAA Paper 1997-2477, 1997.

[12]   Olynick, D., Chen, Y. K., and Tauber, M. E., "Aerothermodynamics of the Stardust Sample Return Capsule," *Journal of Spacecraft and Rockets*, Vol. 36, No. 3, 1999, pp. 442–462.

[13]   Chen, Y. K., Henline, W. D., and Tauber, M. E., "Mars Pathfinder trajectory based heating and ablation calculations," *Journal of Spacecraft and Rockets*, Vol. 32, No. 2, 1995, pp. 225–230.

[14]   Gnoffo, P. A., Weilmuenster, K. J., Braun, R. D., and Cruz, C. I., "Influence of sonic-line location on Mars Pathfinder Probe aerothermodynamics," *Journal of Spacecraft and Rockets*, Vol. 33, No. 2, 1996, pp. 169–177.

[15]   Yamada, T., Abe, T., Yokota, R., Ishida, Y., Ogasawara, T., Suzuki, T., and Fujita, K., *Symposium of Fluid Mechanics and Astrodynamics*, 2007.

[16]   Yamada, T., Ishida, Y., Suzuki, T., Takasaki, K., Fujita, K., Ogasawara, T., and Abe, T., "Development of High and Low Density Ablators for Dash-II and Future Reentry Missions," *Proceedings of the 27th International Symposium on Space Technology and Science*, July 5-12 2009, p. 3.

[17] Isakeit, D., Wilson, A., Watillon, P., Leveugle, T., Cazaux, C., and Bréard, G., "The atmospheric reentry demonstrator," Tech. Rep. BR-138, ESA, October 1998.

[18] Smith, A. J., Parnaby, G. D., Matthews, A. J., and Jones, T. V., "Aerothermodynamic Environment of the Beagle 2 Entry Capsule," *Fourth Symposium on Aerothermodynamics for Space Vehicles*, edited by R. A. Harris, Vol. 487 of *ESA Special Publication*, Feb. 2002, p. 271.

[19] Bouilly, J.-M., Bonnefond, F., Dariol, L., Jullien, P., and Leleu, F., "Ablative thermal protection systems for entry in Mars atmosphere. A presentation of materials solutions and testing capabilities," *4th International Planetary Probe Workshop*, Pasadena, California, July 27-30 2006.

[20] Bouilly, J.-M. and Plaindoux, C., "ASTERM: Maturation of a new low density ablative material," *7th European Workshop on TPS and Hot Structures*, ESA, Noordwijk, Netherlands, April 8-10 2013.

[21] Pinaud, G., Bouilly, J.-M., Barcena, J., Florez, S., Perez, B., Fisher, W., Leroy, V., Bernard, D., Massuti, T., Herdrich, G., Zuber, C., and Rotaermel, W., "HYDRA: Macroscopic modelling of Hybrid Ablative Thermal Protection System," *Proceedings of the 5th International Conference on Porous Media and its Applications in Science and Engineering*, ICPM5, Kona, Hawaii, June 22-27 2014.

[22] Ritter, H., Agnolon, D., and Ferracina, L., "ESA TPS Activities for Sample Return Missions," *9th International Planetary Probe Workshop*, Toulouse, June 18-22 2012.

[23] Ritter, H., Bayle, O., Mignot, Y., Portela, P., Bouilly, J.-M., and Sharda, R., "Ongoing European Developments on Entry Heatshields and TPS Materials," *8th International Planetary Probe Workshop*, Portsmouth, June 6-10 2011.

[24] Conley, J., *"Thermal Protection Materials Branch"*, NASA, August 2014, Retrieved from: `http://www.nasa.gov/content/thermal-protection-materials-branch/#.VVY_-VpN3Hj`.

[25] Institute of Space and Astronautical Science, *"Retrieval of the Hayabusa capsule was completed, Heat shield was found in WPA"*, June 2010, Retrieved from: `http://www.isas.jaxa.jp/e/topics/2010/0614_3.shtml`.

[26] Indian Space Research Organisation, *"LVM3-X/CARE Mission"*, December 2014, Retrieved from: `http://www.isro.gov.in/launchers/lvm3-x-care`.

[27] Laub, B. and Venkatapathy, E., "Thermal Protection System Technology and Facility Needs for Demanding Future Planetary Missions," *International Workshop on Planetary Probe Atmospheric Entry and Descent Trajectory Analysis and Science*, Lisbon, Portugal, October 6-9 2003.

[28] Menees, G., "An evaluation of computer codes for simulating the Galileo Probe aerothermal entry environment," *16th Thermophysics Conference*, AIAA Paper 1981-1069, 1981.

[29] Howe, J., Pitts, W., and Lundell, J., "Survey of the supporting research and technology for the thermal protection of the Galileo Probe," *16th Thermophysics Conference*, AIAA Paper 1981-1068, 1981.

[30] Milos, F. S. and Chen, Y. K., "Ablation, Thermal Response, and Chemistry Program for Analysis of Thermal Protection Systems," *Journal of Spacecraft and Rockets*, Vol. 50, No. 1, 2013, pp. 137–149.

[31] Hoover, R. and Mangini, N., *"NASA Ames Helps Re-enter the Dragon"*, Ames Research Center, NASA, May 2012, Retrieved from: `http://www.nasa.gov/exploration/commercial/cargo/spacex_heatshield.html`.

[32] Lundell, J. H. and Dickey, R. D., "Ablation of ATJ Graphite at High Temperature," *AIAA Journal*, Vol. 11, No. 2, February 1973, pp. 216–222.

[33] Brewer, W. D., "Ablative material response to CO2 laser radiation," *Journal of Spacecraft and Rockets*, Vol. 7, No. 12, 1970, pp. 1449–1453.

[34] Kratsch, K. M., Loomis, W. C., and Randles, P. W., "Jupiter Probe Heat Shield Design," *AIAA/ASME 18th Structures, Structural Dynamics and Material Conference*, AIAA Paper 1977-427, San Diego, California, March 1977.

[35] Wakefield, R. M. and Pitts, W. C., "Analysis of the Heat-Shield Experiment on the Pioneer-Venus Entry Probes," *15th Thermophysics Conference*, AIAA Paper 1980-1494, July 1980.

[36] Balakrishnan, A. and Nicolet, W. E., "Galileo Probe Forebody Thermal Protection: Benchmark Heating Environment Calculations," *16th Thermophysics Conference*, AIAA Paper 1981-1072, June 1981.

[37] Milos, F. S., "Galileo Probe Heat Shield Ablation Experiment," *Journal of Spacecraft and Rockets*, Vol. 34, No. 6, 1997, pp. 705–713.

[38] Moss, J. and Simmonds, A., "Galileo Probe Forebody Flowfield Predictions during Jupiter Entry," *3rd Joint Thermophysics, Fluids, Plasma and Heat Transfer Conference*, AIAA Paper 1982-0874, 1982.

[39] Raiche, G. and Driver, D., "Shock Layer Optical Attenuation and Emission Spectroscopy Measurements During Arc Jet Testing with Ablating Models," *42nd AIAA Aerospace Sciences Meeting and Exhibit*, AIAA Paper 2004-825, 2004.

[40] Kihara, H., Hatano, M., Nakiyama, N., ichi Abe, K., and Nishida, M., "Preliminary Studies of Spallation Particles Ejected from an Ablator," *Transactions of the Japan Society for Aeronautical and Space Sciences*, Vol. 49, No. 164, 2006, pp. 65–70.

[41] Yoshinaka, T., "Spallation Measurement at the Ablator Plasma Wind Tunnel Tests," Tech. Rep. NASDA-TMR-970006E, National Space Development Agency of Japan, Tokyo, February 1998.

[42] Dhanak, A. M., "A theoretical study of mechanical erosion from a charred surface in boundary layer flows," Tech. Rep. AVCO RAD-7-TM-60-74, December 1960.

[43] Scala, S. M. and Gilbert, L. M., "Thermal Degradation of a Char-Forming Plastic During Hypersonic Flight," *ARS Journal*, Vol. 32, No. 6, June 1962, pp. 917–924.

[44] Robbins, D. L., "Thermal Erosion of Ablative Materials," Tech. Rep. TR-61-307, Aeronautical Systems Division, Aerojet General Corporation, April 1962.

[45] Acurex Corporation, *User's Manual Aerotherm Charring Material Thermal Response and Ablation Program*, Vol. 1, Mountain View, California, April 1970.

[46] Mathieu, R. D., "Mechanical Spallation of Charring Ablators in Hyperthermal Environments," *AIAA Journal*, Vol. 2, No. 9, September 1964, pp. 1621–1627.

[47] Schneider, P. J., Dolton, J. A., and Reed, G. W., "Mechanical Erosion of Charring Ablators in Ground-Test and Re-Entry Environments," *AIAA Journal*, Vol. 6, No. 1, January 1968, pp. 64–73.

[48] Dunbar, L. E., Courtney, J. F., and McMillen, L. D., "Heating Augmentation in Erosive Hypersonic Environments," *AIAA Journal*, Vol. 13, No. 7, July 1975, pp. 908–912.

[49] Holden, M. S., Gustafson, G. Q., Duryea, G. R., and Hudack, L. T., "An Experimental Study of Particle-Induced Convective Heating Augmentation," *AIAA 9th Fluid and Plasma Dynamics Conference*, AIAA Paper 76-320, San Diego, California, July 14-16 1976.

[50] Lundell, J. and Dickey, R., "The response of heat-shield materials to intense laser radiation," *16th Aerospace Sciences Meeting*, AIAA Paper 1978-138, 1978.

[51] Lundell, J., "Spallation of the Galileo probe heat shield," *3rd Joint Thermophysics, Fluids, Plasma and Heat Transfer Conference*, AIAA Paper 1982-852, 1982.

[52] Park, C., "Stagnation-point ablation of carbonaceous flat disks. I Theory," *AIAA Journal*, Vol. 21, No. 11, 1983, pp. 1588–1594.

[53] Park, C., "Stagnation-point ablation of carbonaceous flat disks. II Experiment," *AIAA Journal*, Vol. 21, No. 12, 1983, pp. 1748–1754.

[54] Park, C. and Balakrishnan, A., "Ablation of Galileo Probe heat-shield models in a ballistic range," *AIAA Journal*, Vol. 23, No. 2, 1985, pp. 301–308.

[55] Park, C., Lundell, J., Green, M., Winovich, W., and Covington, M., "Ablation of carbonaceous materials in a hydrogen-helium arc-jet flow," *18th Thermophysics Conference*, AIAA Paper 1983-1561, 1983.

[56] Lundell, J., Dickey, R., and Otten, L., "The CO2 gasdynamic laser as a high-intensity radiation facility," *13th Aerospace Sciences Meeting*, AIAA Paper 1975-177, 1975.

[57] Dickey, R. R. and Lundell, J. H., *A Technique for Evaluating the Jovian Entry Probe Heat Shield Material with a Gasdynamic Laser*, No. 79 CH 1500-8 AES, IEEE Publication, September 1979.

[58] Nicolet, W. E., "Radiation Heating Environments for Jovian Entry Conditions," *Progress in Astronautics and Aeronautics, Radiative Transfer and Thermal Control*, edited by A. M. Smith, Vol. 49, AIAA, New York, 1976, pp. 231–250.

[59] Bartlett, E. and Kendall, R., "Thermochemical ablation," *Thermophysics Specialist Conference*, AIAA Paper 1965-642, 1965.

[60] Sullivan, J. and Kobayashi, W., "Spallation modeling in the Charring Material Thermal Response and Ablation (CMA) computer program," *22nd Thermophysics Conference*, AIAA Paper 1987-1516, 1987.

[61] Gakenheimer, D. C., Patterson, D. M., and Wenzel, R. F., "Continuous Wave Laser Tests on Booster Motor Case Materials," *Final Report*, R&D Associates, December 1983, p. 45.

[62] Ziering, M. and Dicristina, V., "Thermomechanical erosion of ablative plastic composites," *7th Thermophysics Conference*, AIAA Paper 1972-299, 1972.

[63] Dolton, T., Goldstein, H., and Maurer, R., "Thermodynamic performance of carbon in hyperthermal environments," *3rd Thermophysics Conference*, AIAA Paper 1968-754, 1968.

[64] Auerbach, I. and McBride, D., "Some observations on the influence of graphite microstructure on ablation performance," *8th Aerospace Sciences Meeting*, AIAA Paper 1970-155, 1970.

[65] Ren, F., Sun, H. S., and Liu, L. Y., "Theoretical analysis for mechanical erosion of carbon-base materials in ablation," *Journal of Thermophysics and Heat Transfer*, Vol. 10, No. 4, 1996, pp. 593–597.

[66] Davies, C. and Park, C., "Trajectories of solid particles spalled from a carbonaceous heat shield," *20th Aerospace Sciences Meeting*, AIAA Paper 1982-200, 1982.

[67] Moss, J. and Kumar, A., "Significance of turbulence and transition location on radiative heating with ablation injection," *19th Aerospace Sciences Meeting*, AIAA Paper 1981-281, 1981.

[68] Lundell, J. and Dickey, R. R., "Response of Heat-Shield Materials to Intense Laser Radiation," *Outer Planet Entry Heating and Thermal Protection*, American Institute of Aeronautics and Astronautics, 1979, pp. 193–209.

[69] Park, C., "Interaction of Spalled Particles with Shock Layer Flow," *Journal of Thermophysics and Heat Transfer*, Vol. 13, No. 4, 1999, pp. 441–449.

[70] Park, C., Raiche, G. A., and Driver, D. M., "Radiation of Spalled Particles in Shock Layers," *Journal of Thermophysics and Heat Transfer*, Vol. 18, No. 4, 2004, pp. 519–526.

[71] Pace, A., Ruffin, S., and Barnhardt, M., "A Coupled Approach for Predicting Radiation Attenuation in Particle-Laced Flows," *42nd AIAA Thermophysics Conference*, AIAA Paper 2011-3771, 2011.

[72] Wright, M. J., Candler, G. V., and Bose, D., "Data-Parallel Line Relaxation Method for the Navier-Stokes Equations," *AIAA Journal*, Vol. 36, No. 9, 1998, pp. 1603–1609.

[73] Whiting, E. E., Park, C., Arnold, J. O., and Paterson, J. A., "NEQAIR96, Nonequilibrium and Equilibrium Radiative Transport and Spectra Program: User's Manual," Tech. Rep. NASA RP-1389, December 1996.

[74] Nozawa, S., Kihara, H., and ichi Abe, K., "Numerical Investigation of Spalled Particle Behavior Ejected from an Ablator Surface," *Transactions of the Japan Society for Aeronautical and Space Sciences*, Vol. 8, No. ists27, 2010, pp. Pe_9–Pe_14.

[75] Esser, B., Gulhan, A., Koch, U., Keller, K., and Beversdorff, M., "Dust Particle Effect on TPS Qualification for Martian Atmosphere," *The 6th European Symposium on Aerothermodynamics for Space Vehicles*, No. ESA SP-659, Versailles, France, January 2009.

[76] Esser, B., Gulhan, A., Koch, U., and Keller, K., "Particle Erosion Tests on an Ablative Material in Martian Atmosphere," *6th European Workshop on Thermal Protection Systems and Hot Structures*, Stuttgart, Germany, April 2009.

[77] MacDonald, M., Jacobs, C., and Laux, C., "Interaction of Air Plasma With Ablating Heat Shield Material," *IEEE Transactions on Plasma Science*, Vol. 42, No. 10, Oct 2014, pp. 2658–2659.

[78] European Space Agency, *"EDM Thermal Protection System Tests"*, October 2010, Retrieved from: `http://exploration.esa.int/mars/49134-edm-thermal-protection-system/`.

[79] Zhang, H.-B., Weng, H., and Martin, A., "Simulation of Flow-tube Oxidation on the Carbon Preform of PICA," *52nd AIAA Aerospace Sciences Meeting*, AIAA Paper 2014-1209, National Harbor, MD, 13-17 January 2014.

[80] Vasilevskii, È. B., Dombrovskii, L. A., Mikhatulin, D. S., and Polezhaev, Y. V., "Heat transfer in the neighborhood of the stagnation point under conditions of hypersonic heterogeneous slip flow past bodies," *High temperature*, Vol. 39, No. 6, 2001, pp. 860–873.

[81] Henderson, C. B., "Drag Coefficients of Spheres in Continuum and Rarefied Flows," *AIAA Journal*, Vol. 14, No. 6, June 1976, pp. 707–708.

[82] Wilke, C. R., "A viscosity equation for gas mixtures," *Journal of Chemical Physics*, Vol. 18, 1950, pp. 517–519.

[83] Blottner, F. G., Johnson, M., and Ellis, M., "Chemically Reacting Viscous Flow Program for Multi-Component Gas Mixtures," Tech. Rep. SC-RR-70-754, Sandia National Laboratories, Albuquerque, NM, 1971.

[84] Vincenti, W. G. and Kruger, C. H., *Introduction to physical gas dynamics*, Wiley, New York, 1965.

[85] Carlson, D. J. and Hoglund, R. F., "Particle Drag and Heat Transfer in Rocket Nozzles," *AIAA Journal*, Vol. 2, No. 11, November 1964, pp. 1980–1984.

[86] Park, C., *Nonequilibrium Hypersonic Aerothermodynamics*, Wiley, New York, 1990.

[87] Chase, Jr., M. W., Davis, C. A., J. R. Downey, J., Frurip, D. J., McDonald, R. A., and Syverud, A. N., "JANAF Thermochemical Tables," *Journal of Physical and Chemical Reference Data*, Vol. 14, 1985.

[88] Baker, R. L., "Graphite Sublimation Chemistry Nonequilibrium Effects," *AIAA Journal*, Vol. 15, No. 10, October 1977, pp. 1391–1397.

[89] Pflieger, R., Sheindlin, M., and Colle, J. Y., "Advances in the Mass Spectrometric Studies of the Laser-Induced Vaporisations of Graphit and Uranium Dioxide," *European Conference on Thermophysical Properties*, Bratislava, Slovak Republic, September 5-8 2005.

[90] Palmer, H. B. and Shelef, M., *Vaporization of Carbon*, Vol. 4 of *Chemistry & Physics of Carbon*, Marcel Dekker, Inc., New York, 1968.

[91] Driver, D. M. and MacLean, M., "Improved predictions of PICA Recession in Arc Jet Shear Tests," *49th AIAA Aerospace Sciences Meeting*, AIAA Paper 2011-141, January 2011.

[92] Maclean, M., Marschall, J., and Driver, D. M., "Finite-Rate Surface Chemistry Model, II: Coupling to Viscous Navier-Stokes Code," *42nd AIAA Thermophysics Conference*, AIAA Paper 2011-3784, June 2011.

[93] Salari, K. and Knupp, P., "Code Verification by the Method of Manufactured Solutions," Tech. Rep. SAND 2000-1444, Sandia National Laboratories, Albuquerque, NM, June 2000.

[94] Roy, C., Ober, C., and Smith, T., "Verification of a Compressible CFD Code Using the Method of Manufactured Solutions," *32nd AIAA Fluid Dynamics Conference and Exhibit*, AIAA Paper 2002-3110, 2002.

[95] Martin, A. and Boyd, I., "Modeling of heat transfer attenuation by ablative gases during the Stardust re-entry," *50th AIAA Aerospace Sciences Meeting including the New Horizons Forum and Aerospace Exposition*, AIAA Paper 2012-814, 2012.

[96] Park, C. and Bogdanoff, D. W., "Shock Tube Measurement of Coefficient of Reaction of Nitrogen Atoms and Solid Carbon: Preliminary Results," *41st Aerospace Sciences Meeting and Exhibit*, AIAA Paper 2003-0158, January 2003.

[97] Goldstein, H. W., "The reaction of active nitrogen with graphite," *The Journal of Physical Chemistry*, Vol. 68, No. 1, 1964, pp. 39–42.

[98] Suzuki, T., Fujita, K., Ando, K., and Sakai, T., "Experimental Study of Graphite Ablation in Nitrogen Flow," *Journal of Thermophysics and Heat Transfer*, Vol. 22, No. 3, 2008, pp. 382–389.

[99] Suzuki, T., Fujita, K., and Sakai, T., "Graphite Nitridation in Lower Surface Temperature Regime," *Journal of Thermophysics and Heat Transfer*, Vol. 24, No. 1, 2010, pp. 212–215.

[100] Suzuki, T., Fujita, K., and Sakai, T., "Numerical Analysis of Graphite Ablation in Nitrogen Flow," *46th AIAA Aerospace Sciences Meeting and Exhibit*, AIAA Paper 2008-1217, 2008.

[101] Suzuki, T., Fujita, K., and Sakai, T., "Experimental Study of Graphite Ablation in Nitrogen Flow, Part II: Further Numerical Analysis," *Journal of Thermophysics and Heat Transfer*, Vol. 24, No. 3, 2010, pp. 589–597.

[102] Zhang, L., Pejakovic, D. A., Marschall, J., Dougherty, M., and Fletcher, D., "Laboratory Investigation of the Active Nitridation of Graphite by Atomic Nitrogen," *Journal of Thermophysics and Heat Transfer*, Vol. 26, No. 1, 2012, pp. 10–21.

[103] Zhang, H.-B., *High Temperature Flow Solver For Aerothermodynamics Problems*, Ph.D. thesis, University of Kentucky, Lexington, Kentucky, 2015.

[104] Majid, A., *Two phase flow solver for solid particles in hypersonic Martian entry flows*, Ph.D. thesis, Universität Stuttgart, Stuttgart, Germany, 2011.

Raghava Sai Chaitanya Davuluri

Education

Bachelor of Engineering in Mechanical Engineering $2006 - 2010$

Osmania University,

Hyderabad, India.

Awards

- *Second Place* in Graduate Research Competition, 99th Annual Meeting of Kentucky Academy of Science, Morehead, KY, 2013

- *Master Certificate in Computer Aided Tool Engineering*, Central Institute of Tool Design, Hyderabad, India, 2011.

Publications

Articles in Refereed Journals

- Davuluri, R. S. C., Zhang, H.-B., and Martin, A., "Numerical study of spallation phenomenon in an arc-jet environment," *Journal of Thermophysics and Heat Transfer*, Vol. 29, No. 3, July 2015.
  DOI: 10.2514/1.T4586

In Preparation

- Martin, A., Bailey, S. C. C., Panerai, F., Davuluri, R. S. C., Vazsonyi, A. R., Zhang, H.-B., Lippay, Z. S., Mansour, N. N., Inman, J. A., Bathel, B. F., Splinter, S. C., and Danehy, P. M., "Overview and preliminary numerical and experimental analysis of the spallation phenomenon," *CEAS Space Journal*, 2015, In preparation (July 2015 Estimated).

Articles in Refereed Conference Proceedings

- Davuluri, R. S. C., Zhang, H.-B., and Martin, A., "Effects of spalled particles thermal degradation on a hypersonic flow field environment", *AIAA Science and Technology Forum and Exposition*, Abstract Submitted (Control ID: 2322154), San Diego, CA, January 2016.

- Martin, A., Bailey, S. C. C., Panerai, F., Davuluri, R. S. C., Vazsonyi, A. R., Zhang, H.-B., Lippay, Z. S., Mansour, N. N., Inman, J. A., Bathel, B. F., Splinter, S. C., and Danehy, P. M., "Preliminary numerical and experimental analysis of the spallation phenomenon," 8th *European Symposium on Aerothermodynamics for Space Vehicles*, Lisbon, Portugal, March 2015.
  DOI: 10.13140/RG.2.1.1612.4328

- Davuluri, R., and Martin, A., "Numerical study of spallation phenomenon in an arc-jet environment," 11th *AIAA/ASME Joint Thermophysics and Heat Transfer Conference*, AIAA Paper 2014-2249, Atlanta, GA, June 2014.
  DOI: 10.2514/6.2014-2249

Refereed Abstracts and Presentations

- Davuluri, R., and Martin, A., "Numerical Study of Spalled Particle Trajectory in an Arc-jet environment," 39th *AIAA Dayton-Cincinnati Aerospace Sciences Symposium*, Dayton, Ohio, March 2014.

- Davuluri, R., and Martin, A., "Simulation of Spallation Phenomenon in a High Enthalpy Argon Arc-jet Flow Environment," 99th *Annual Meeting of Kentucky Academy of Science*, Morehead, Kentucky, November 2013.

- Davuluri, R., and Martin, A., "Numerical Simulation of Spallation Phenomenon in an Arc-jet environment," 38th *AIAA Dayton-Cincinnati Aerospace Sciences Symposium*, Dayton, Ohio, March 2013.

Poster Presentations

- Davuluri, R. S. C., Zhang, H.-B., and Martin, A., "Effectiveness of spalled particles on the flow field environment," *2015 KY EPSCOR Annual Conference*, Lexington, Kentucky, May 2015.

- Davuluri, R., and Martin, A., "Numerical Modeling of Spalled Particle Trajectory in an Arc-Jet Environment," 6th *Ablation Workshop*, Urbana-Champaign, Illinois, April 2014.

- Davuluri, R., and Martin, A., "Numerical Simulation of Spalled Particle Trajectory in an Arc-jet Environment," *2013 KY EPSCOR Annual Meeting*, Louisville, Kentucky, October 2013.

- Davuluri, R., "Neem as a Bio Diesel", *INNOVATIONS*, Hyderabad, India, March 2007.

Others

- <u>Davuluri, R.</u>, CAD Model of "Speed Reducer", *National Level Solid Modeling Contest*, Hyderabad, India, March 2009.